

TESTS OF SHOCK CHEMISTRY IN IC 443G

B. E. TURNER

National Radio Astronomy Observatory,¹ 520 Edgemont Road, Charlottesville, VA 22903

KIN-WING CHAN

Astronomy Department, University of Maryland, College Park, MD 20742

S. GREEN

NASA/Goddard Space Flight Center, Institute for Space Studies, 2880 Broadway, New York, NY 10025

AND

D. A. LUBOWICH

Department of Physics and Astronomy, Hofstra University, Hempstead, NY 11550; and
 American Institute of Physics, 500 Sunnyside Boulevard, Woodbury, NY 11797

Received 1992 February 11; accepted 1992 May 4

ABSTRACT

A multitransition single-dish study has been made of the molecular species CO, HCO⁺, HCN, CN, SiO, CS, SO, and H₂CO toward the “shocked” clump IC 443G associated with the supernova remnant IC 443. Maps of each molecule show source sizes $\geq 40''$ and essentially uniform brightness. A BIMA interferometer map of the 1–0 transition of HCO⁺ shows four small clumps, whose combined flux is only 4.5% of the single-dish flux, so that they represent only small enhancements of an otherwise smooth distribution. A BIMA map of the 86 GHz transition of SO detected no emission to a level of 0.518 Jy beam⁻¹, indicating no clumping on size scales up to 21'', the beamwidth of the single-dish observations.

The observations have been analyzed by both large velocity gradient and microturbulent radiative transfer models, from which densities, temperatures, and abundances are inferred. These models used collision rates calculated in detail for every species except CN and SO, including new collision rates calculated for SiO at low temperatures (40–300 K) and for CS at higher temperatures (100–300 K) than previously existed. We find that the eight species may be divided into two groups. Group 1 species (CO, HCO⁺, HCN, CN) arise in region 1 with density $n \sim (2\text{--}8) \times 10^5 \text{ cm}^{-3}$, temperature $T \leq 100 \text{ K}$, and linear extent $L \approx 7 \times 10^{17} \text{ cm}$, while group 2 species (SiO, CS, SO, H₂CO) arise in the hotter ($T = 200\text{--}300 \text{ K}$), denser ($n \geq 10^6 \text{ cm}^{-3}$) region 2 with smaller L . While abundances of group 1 species are consistent with ion-molecule chemistry, the observed abundances of group 2 species, if they are coextensive with group 1 species, are much lower than predicted ion-molecule abundances, and in addition the observed line widths are all much larger than those of quiescent clouds where ion-molecule processes are believed to dominate. We find that dissociative (D) shock models of Neufeld & Dalgarno (1989) agree well with observed abundances of group 1 species, while nondissociative (ND) shock models (Mitchell 1984a, b; Hartquist, Oppenheimer, & Dalgarno 1980) explain group 2 abundances well. Specifically, both observations and D shock models show that abundances of group 1 species are in no cases enhanced by shocks over quiescent cloud conditions, while both observations and ND shock models show that abundances of group 2 species are all reduced below quiescent cloud (ion-molecule) abundances as a result of shocks unless they occupy a region ~ 100 times smaller than group 1 species, in which case their fractional abundances are similar to those of ion-molecule chemistry.

In general, observed line widths vary inversely with derived excitation density, while centroid velocities of all species are essentially identical. This requires that the shock velocity v_c in the clump varies along the path z , rising quasi-symmetrically from a small value at $z = 0$ (rear face of the clump) to a maximum value in region 1, then decreasing to a value consistent with a ND shock in region 2 (near face of clump). The density gradient necessary to produce the v_c function must have preceded the shock. All physical and chemical properties can be explained satisfactorily on this picture of the IC 443G clump, but it is ad hoc, and more detailed models of shocks in nonhomogeneous media are needed.

Subject headings: H II regions — ISM: individual (IC 443) — ISM: molecules — molecular processes — shock waves

1. INTRODUCTION

Despite many observations of several molecular species toward a variety of interstellar sources believed to contain shocks, no definite assessment of the role of shocks in the chemistry has yet been possible. Species of S and Si are commonly considered the best tests, since they have been observed

with “enhanced” abundances in warm or energetic sources and thus are believed to involve high temperatures. Thus the observation (Ziurys, Friberg, & Irvine 1989b) that the SiO/HCN ratio appears to increase with kinetic temperature T_k for a limited sample of molecular clouds is argued to imply that SiO forms via endothermic reactions which have activation barriers of $\sim 90 \text{ K}$. However, Turner (1991a) argues that evaporation of only 4% of the refractory ice mantles (at 90 K) in warm regions produces exactly the observed abundance of

¹ Operated by Associated Universities, Inc., under cooperative agreement with the National Science Foundation.

both SiO and PN in the energetic Orion-KL core. The detection of SiO emission in the core of the B1 and L1448 clouds with $T_k \approx 14$ K (Bachiller et al. 1990; Bachiller, Martín-Pintado, & Fuente 1991) casts doubt on a general dependence of the SiO abundance on T_k as found in other clouds and suggests formation of SiO by ion-molecule reactions (cf. Herbst et al. 1989). A more detailed study of SiO toward the outflow sources in L1448, B1, NGC 2071, and Cep A (Martín-Pintado, Bachiller, & Fuente 1992) shows that the quiescent gas has a fractional abundance $X(\text{SiO}) < 4 \times 10^{-12}$, 2 times higher than the upper limit in the cold TMC-1 core (Ziurys et al. 1989b), but rises to values of 2×10^{-6} near the exciting star in L1448, implying that at least 3% of Si is in the gas phase. The question remains, however, whether the enhanced SiO is formed in a hot phase (shocks) or by desorption of refractory ice mantles on grains. Our study of the simple shocked clump IC 443G shows that a much smaller fractional abundance is to be expected from shocks, and hence that the large abundance of SiO in L1448 and other outflow sources may well arise from evaporative mechanisms.

Sulfur species are equally ambiguous. Many S species are commonly observed in the cold TMC-1 source, so ion-molecular processes certainly occur. In energetic sources such as Orion-KL the enhanced abundances (a factor of 10–200 above TMC-1) are again explainable by the desorption of only a few percent of refractory ice mantles (Turner 1991a), but also may occur via high-temperature gas-phase reactions. One argument in favor of the grain desorption process is that SO and SO₂ are observed with the same abundances in Orion-KL, while all shock models (Hartquist, Oppenheimer, & Dalgarno 1980; Neufeld & Dalgarno 1989) predict a ratio $\text{SO}/\text{SO}_2 \geq 1000$. Grain processes, conversely, would be expected to convert SO into SO₂.

The shocked clumps near IC 443 offer a unique test of grain versus shock chemistry, for several reasons. First, they are uncontaminated by outflows from star formation, by ionized gas in an H II region, or by warm atomic gas from a photo-dissociation region. Thus we may assume that clumps such as IC 443G are initially cold, dense molecular cores subsequently impacted by the shock wave from the supernova which occurred $\sim (4\text{--}13) \times 10^3$ yr ago (Parkes et al. 1977). Gentle grain mantle evaporation, such as apparently produced at least some of the complex species seen in Orion-KL, seems not to have occurred in IC 443G, judging from our unsuccessful searches for them (§ 3.9). Second, the analysis of H₂CO, recently discovered in IC 443G (Turner & Lubowich 1991) shows that the H₂CO gas is very hot (> 300 K), the first direct determination of a high temperature in dense molecular gas in a shocked source. Owing to the absence of other energetic phenomena, we can assume that the high temperature is a direct consequence of a shock.

A complication in assessing shock chemistry is that shocks may be nondissociating (Iglesias & Silk 1978; Hartquist et al. 1980; Mitchell 1984a, b) or dissociating (Neufeld & Dalgarno 1989), with corresponding differences in predicted abundances. Thus one could adopt two approaches to testing shock chemistry models. The first is the standard determination of abundances of key species chosen to best test shock models. A possible limitation here is beam dilution. Our combination of single-dish maps at 20'' resolution and interferometry of two species (HCO⁺, SO) is designed to minimize this possibility. A second approach would be to observe a class of species (SO, SO₂, CN, HCN) whose predicted abundances are the same for

both nondissociating and dissociating shocks, then derive an effective beam dilution for these and apply it to a second class of species (SiO, H₂CO, HCO⁺, C₃H₂) whose predicted abundances are very different for the two shock types. This amounts to a "relative abundance" comparison of observations with models, and checks the internal consistency of the models independent of possible beam-dilution effects so long as the species in question are coextensive. Because the first approach concludes that the observed species group into two non-coextensive regimes, the second approach is not useful.

A single-dish multispecies study at single positions near IC 443B and IC 443G was made earlier by Ziurys, Snell, & Dickman (1989a), who assumed no beam dilution and values of T much lower than deduced by Turner & Lubowich (1991) from their H₂CO observations. The LTE analysis of Ziurys et al. (based on only single transitions of most species) yielded values of X/HCN typical of the cold cloud TMC-1, where $X = \text{HCO}^+$, N_2H^+ , CS, SO, SiO, HCN, CN, NH₃. The very different physical conditions deduced from H₂CO have prompted us to reevaluate the molecular abundances in IC 443G by obtaining maps, multiple transitions for each species, and interferometry for HCO⁺ and SO.

2. OBSERVATIONS AND RESULTS

2.1. Single-Dish Results

All single-dish observations were made with the NRAO 12 m telescope over several observing sessions from 1990 December to 1991 November. At both 1.3 and 3 mm the receiver consisted of dual-channel cooled SIS detectors, operating in double-sideband and single-sideband modes, respectively. The product of forward and rear spillover efficiencies is $\eta_f \eta_{\text{rss}} \approx 0.64$ at all frequencies. At 90 GHz the beam size and main-beam efficiency are $\theta_B = 67''$, $\eta_c = 0.64$, respectively, and at 230 GHz they are 26.5'' and 0.39. Exact values for each observed frequency are used in converting measured (corrected) temperatures T_R^* to brightness temperatures via $T_B = T_R^*/\eta_c \eta_f$, where η_f is the geometric main beam dilution factor. The T_R^* calibration scale is checked by a spectral-scan observation of Jupiter in both wavelength bands. Pointing was checked every 2 hr on Jupiter, which was always within 10° of IC 443. The pointing varied by at most 6'' between determinations, producing negligible effect on observed line intensities. All data were obtained by position-switching the telescope every 30 s by 15' in azimuth. Spectral resolutions were 1 MHz at 3 mm wavelength and 2 MHz at 1.3 mm (except CS $J = 5\text{--}4$ at 244 GHz, which is 1 MHz).

The data are given in Table 1. The central position (0, 0) is R.A. = 06^h13^m42^s.1, decl. = 22°33'30" (1950), determined by G. Mitchell (1990, private communication) as the position of peak intensity of the HCO⁺ $J = 3\text{--}2$ line. Estimated errors are $\sim 2.5 \sigma$ for the (0, 0) positions, somewhat higher ($\sim 2 \sigma$) for the offset positions.

In Figure 1a we present aligned spectra of the species at 1.3 mm in order to compare the profile centroids and widths. The spectra are of the (0, 0) position but are virtually the same at the other positions. These spectra show that the line width decreases in the order CO, HCO⁺, HCN, CN, SiO, (H₂CO, SO, CS), where the species in parentheses are indistinguishable. Similarly, the 3 mm spectra are plotted in Figure 1b. Here HCN and CN are complicated by resolved hyperfine structure (hfs). Line widths at 3 mm are identical with 1.3 mm line widths, except possibly for CS, which shows a low-velocity

TABLE 1
SINGLE-DISH OBSERVATIONS OF IC 443G

Species	Transition	Frequency (GHz)	Position ^a	T_R^* (K)	v (km s ⁻¹)	Δv (km s ⁻¹)	Resolution ^b (km s ⁻¹)
A. 1.3 mm Results							
HCO ⁺	$J = 3-2$	267.55762	(0, 0) (20, 0) (-20, 0) (0, 20) (0, -20) (0, -40)	0.72 ± 0.08 0.60 0.58 0.56 0.68 0.525	-6.6 ± 1.5 -8.9 -6.6 -6.6 -6.6 -6.6	22.4 ± 2 23.3 19.0 21.3 20.6 19.7	2.24
HCN	$J = 3-2$	265.88643	(0, 0) (20, 0) (-20, 0) (-40, 0) (0, 20) (-20, 20) (0, -20) (-20, -20)	0.62 ± 0.05 0.18 0.81 0.2 0.58 0.41 0.39 0.60	-8.4 ± 1.5 -8.4 -8.4 ~ -6.1 -8.4 -7.3 -8.4 -7.3	18.0 ± 2 12.4 16.9 15.1 18.9 18.3 18.5 17.4	2.26
CN	$N = 2-1, J = 5/2-3/2,$ $F = 5/2-3/2, 7/2-5/2, 3/2-1/2^c$	226.875	(0, 0) (20, 0) (-20, 0) (0, 20) (0, -20) (0, -40) (0, -60)	0.40 ± 0.04 0.21 0.21 0.25 0.53 0.61 0.23	-7.9 ± 1.7 -6.6 -5.3 -7.9 -7.9 -7.9 -7.9	11.9 ± 2.2 13.2 11.6 17.4 10.6 10.6 14.5	2.64
SiO	$J = 5-4$	217.10493	(0, 0) (20, 0) (-20, 0) (0, 20) (0, -20) (0, -40) (0, -60)	0.23 ± 0.03 0.11 0.12 0.16 0.17 0.15 <0.03	-10.1 ± 1.7 -10.1 -7.3 -10.1 -7.3 -7.3 ...	14.9 ± 2.2 16.0 12.4 13.3 13.3 15.5 ...	2.76
CS	$J = 5-4$	244.93561	(0, 0) (20, 0) (-20, 0) (0, 20) (0, -20) (0, -40) (0, -60)	0.29 ± 0.05 0.28 ~0.12 0.21 0.39 0.36 ~0.12	-7.6 ± 1.5 -7.6 ... -10.0 -6.3 -7.6 ...	11.6 ± 2 10.8 _d ~16.0 ^d 10.5 12.2 _d	1.22
SO	6_5-5_4	219.94939	(0, 0) (20, 0) (-20, 0) (0, 20) (0, -20) (0, -40) (0, -60)	0.32 ± 0.04 0.12 0.21 0.21 0.32 0.26 ~0.04	-6.7 ± 1.5 -6.7 -6.7 -6.7 -6.7 -6.7 ...	13.1 ± 2 14.4 12.0 13.1 12.2 13.6 ...	2.72
SO	5_5-4_4	215.22065	(0, 0) (0, -20) (0, -40) (0, -60)	0.185 ± 0.04 0.15 0.15 <0.04	-9.1 ± 1.5 -6.3 -3.5 ...	12.8 ± 2 16.4 15.3 ...	2.78
H ₂ CO	$3_{03}-2_{02}$	218.22219	(0, 0) (0, -20) (0, -40) (0, -60)	0.18 ± 0.02 0.15 0.16 <0.04	-7.0 ± 1.5 -5.6 -7.0 ...	13.2 ± 2.2 15.9 13.2 ...	2.74
B. Results							
HCO ⁺	$J = 1-0$	89.18852	(0, 0)	2.1 ± 0.1	$-8.4^e \pm 2$	24.3 ± 2	1.68
HCN	$J = 1-0$	88.63160	(0, 0)	$1.56^f \pm 0.1$	-8.3 ± 2.2	20.7 ± 2.2	1.69
CN ^g	$N = 1-0, J = 3/2-1/2,$ $F = 3/2-1/2, 5/2-3/2$	113.490	(0, 0) (20, 0) (-20, 0) (0, -20) (0, -40) (0, -60)	0.39 ± 0.03 0.21 0.49 0.43 0.27 0.19	-6.3 ± 1.3 -6.9 -6.3 -7.6 -6.9 -6.9	15.8 ± 2 15.8 16.5 15.0 15.8 15.8	1.32
SiO	$J = 2-1$	86.84700	(0, 0) (20, 0) (-20, 0)	0.12 ± 0.02 0.11 0.10	-8.3 ± 1.7 -9.1 -8.7	14.3 ± 1.7 13.8 15.5	1.73

TABLE 1—Continued

Species	Transition	Frequency (GHz)	Position ^a	T_R^* (K)	v (km s ⁻¹)	Δv (km s ⁻¹)	Resolution ^b (km s ⁻¹)
CS	$J = 2-1$	97.98097	(0, 20)	0.15	-9.1	17.1	1.53
			(0, -20)	0.10	-8.3	12.9	
			(0, -40)	0.05	
			(0, 0)	0.47 ± 0.04	-6.9 ± 1.5	11.6 ± 1.5	
			(20, 0)	0.36	-7.7	11.8	
			(-20, 0)	0.55	-6.2	10.8	
			(0, -20)	0.62	-6.6	11.2	
			(0, -40)	0.63	-6.6	11.3	
SO	3_2-2_1	99.29988	(0, -60)	0.38	-6.2	11.9	1.51
			(0, 0)	0.165 ± 0.02	-7.0 ± 1.5	10.0 ± 1.5	
			(20, 0)	0.10	-5.5	11.4	
			(-20, 0)	0.19	-7.0	10.2	
			(0, -20)	0.19	-7.7	11.2	
SO	2_2-1_1	86.09394	(0, 0)	0.023	
SO	2_3-1_2	109.25218	(0, 0)	0.034	

^a Offsets in arcseconds.^b Maximum uncertainty in v and Δv ; the uncertainty is usually ~ 0.5 resolution elements.^c These three hf components have the same frequency within 0.4 resolution elements.^d Relatively poor signal-to-noise ratio.^e Uncertainty due to self-absorption.^f Summed over the hf components deduced from Gaussian deconvolution.^g Intensity is that of the $F = 3/2-1/2$, $5/2-3/2$ blend, for which a reliable deconvolution is not possible.

wing at 3 mm, and SO, for which Δv at 1.3 mm possibly exceeds Δv at 3 mm. CO results are from White et al. (1987). In § 3 we show that the density derived from excitation analyses generally increases in the same order as the line widths decrease, and also is identical for SO and H_2CO , which have the largest n .

2.2. Interferometry

Observations of the $J = 1-0$ transition of HCO^+ (89.188 GHz) and the 2_2-1_1 transition of SO (86.094 GHz) were made simultaneously of IC 443G with the Hat Creek three-element interferometer in B-array configuration, during 1990 October to 1991 January.² Data from five configurations were obtained. The 512 channel digital correlator was configured in eight spectral windows of 64 channels each, of spacing 0.625 MHz (2.1 km s⁻¹ resolution at 89 GHz). Synthesis maps were prepared using the newly developed MIRIAD software, map sizes being 128×128 pixels of cell size $3'' \times 3''$. The synthesized beam is $15.4'' \times 8.3''$, comprising 15 baselines covering 13–94 m. The primary beamwidth is $142''$. Total integration time was 65.4 hr.

Figure 2 shows the maps of HCO^+ $J = 1-0$. Emission from the four detected clumps dominates the -13.4 , -11.2 and -9.0 km s⁻¹ maps. Figure 3 shows the spectra for each clump. The FWHM line widths range from 6.6 to 9.4 km s⁻¹, much narrower than the 24 km s⁻¹ width of the single-dish profile. None of the spectra individually show the narrow self-absorbed spike component at $v_{LSR} = -5$ km s⁻¹, present in the single-dish HCO^+ $J = 1-0$ profile and also in the CO $J = 2-1$ (White et al. 1987) and $1-0$ (DeNoyer & Frerking 1981) spectra. This narrow component, of width 3 km s⁻¹, appears to be a cooler foreground cloud, although its line

width is too large to suggest a cold dense cloud, and it is likely connected in some way to the energetics of the IC 443G clump. The peak brightness temperatures of the clumps and their corresponding velocities and positions are as follows: (clump 1, 1.83 K, -9.0 km s⁻¹, R.A. $06^h13^m40^s.1$, decl. $22^\circ32'34''$; clump 2, 1.83 K, -11.2 km s⁻¹, R.A. $06^h13^m41^s.15$, decl. $22^\circ33'23''$; clump 3, 1.42 K, -13.4 km s⁻¹, R.A. $06^h13^m42^s.5$, decl. $22^\circ34'00''$; clump 4; 0.98 K, -9.0 km s⁻¹, R. A. $06^h13^m40^s.0$, decl. $22^\circ34'04''$). These brightness temperatures are comparable to the single-dish values of 3.3 K for $J = 1-0$ (averaged over the $72''$ main beam), and 2.2 K for $J = 3-2$ ($24''$ beam). Thus the small clumps represent only modest excursions in brightness from an otherwise fairly smooth brightness distribution.

The four HCO^+ clumps represent only 4.5% of the total single-dish flux. In Figure 1b we have plotted the sum of the fluxes from the four clumps on the single-dish profile. A conversion of 31 Jy K⁻¹ has been used for the 12 m telescope at 89.1 GHz. None of the clumps is appreciably attenuated by the primary-beam response of BIMA, while clump 1 is attenuated $\sim 75\%$ and clumps 2 and 3 $\sim 50\%$ in the $72''$ 12 m telescope beam, but in any case these contribute a negligible fraction of the total flux. The truncated nature of the low-velocity side of the aggregate clump spectrum suggests the presence of the foreground absorption at -5 km s⁻¹.

The BIMA results for the SO 2_2-1_1 transition at 86.094 GHz are negative. The 3σ upper limit on the line intensity is 0.518 Jy beam⁻¹, corresponding to $T_B = 0.75$ K for each of the 16 channel maps covering the velocity range $-17.80 + 15.20$ km s⁻¹. An important question is the minimum possible spatial size of an SO source that is consistent with our upper limits. To estimate this, we start with our single-dish observation of the SO 3_2-2_1 transition at 99.299 GHz, which yields $T_R^* = 165$ mK (Table 1), or $T_B \approx T_R^*/\eta_c = 266$ mK, corresponding to 9.58 Jy beam⁻¹ for the 12 m telescope. At the high densities that characterize the SO excitation (§ 3), the corresponding SO 2_2-1_1 transition should produce $T_B = 0.10$ K. Our actual observation

² The BIMA array is operated by the Berkeley-Illinois-Maryland Association with support from the National Science Foundation under grant AST-9100306 and the State of Maryland through its contributions to the Laboratory for Millimeter-Wave Astronomy.

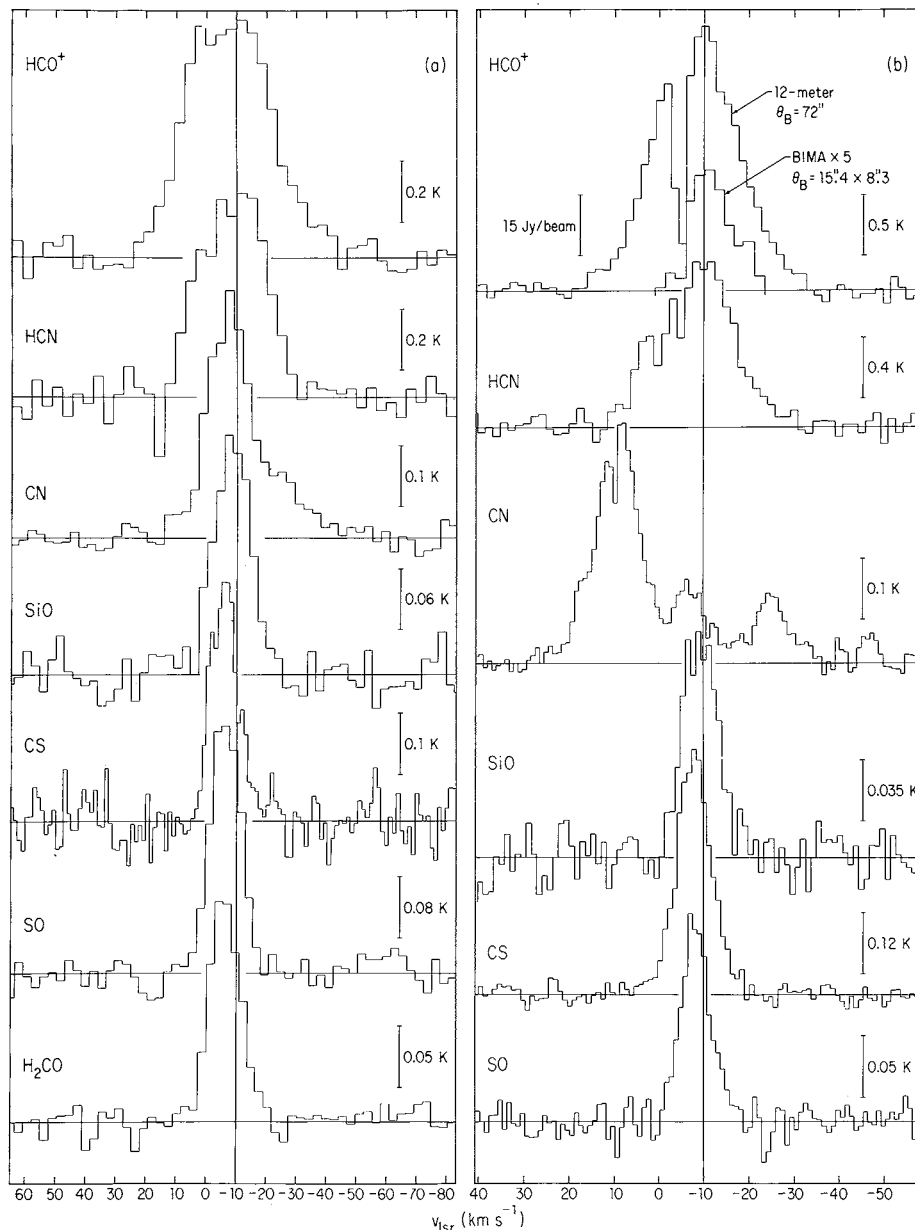


FIG. 1.—(a) 1.3 mm single-dish spectra at position (0, 0): R.A. = $06^{\text{h}}13^{\text{m}}42^{\text{s}}.0$; decl. = $22^{\circ}33'30''$ (1950). The T_{R}^* temperature scale is shown. Transitions are HCO^+ ($J = 3-2$); HCN ($J = 3-2$); CN ($N = 2-1$, $J = 5/2-3/2$, $F = 5/2-3/2$, $7/2-5/2$, $3/2-1/2$ [blended]); SiO ($J = 5-4$); CS ($J = 5-4$); SO ($N_J = 6_5-5_4$); H_2CO ($3_{03}-2_{02}$). Line widths decrease from top to bottom but are virtually identical for SiO , CS , SO , H_2CO , which all arise in the denser region 2 (see text). (b) 3 mm single-dish spectra at position (0, 0). Transitions are HCO^+ ($J = 1-0$); HCN ($J = 1-0$, hfs blended); CN ($N = 1-0$, $J = 3/2-1/2$, $F = 3/2-1/2$, $5/2-3/2$ [blended], $1/2-1/2$, $3/2-3/2$, $1/2-3/2$); SiO ($J = 2-1$); CS ($J = 2-1$); SO ($N_J = 3_2-2_1$). Strong foreground absorption is seen at -5 km s^{-1} in all group 1 species (CO [White et al. 1987], HCO^+ , HCN , and CN). The absorption allows the velocity of HCN and CN to be determined in the presence of blended hf components. The absorption is not seen in group 2 species at 3 mm, because the lower states of their observed transitions are not ground states. The high-velocity blue wing is seen prominently in HCO^+ and CN , and possibly in HCN . On the HCO^+ spectrum is superposed the composite spectrum of the four small clumps detected with the BIMA array. They comprise only 4.5% of the single-dish flux.

gives $T_{\text{R}}^* = 23.3 \text{ mK}$, or $T_{\text{B}} = 0.037 \text{ K}$, corresponding to a flux of $1.20 \text{ Jy beam}^{-1}$ in the $75''$ 12 m telescope beam. Because the interferometer contained several short spacings, it responds to sources of size much larger than the synthesized beam, but with diminished sensitivity. We have used the UVGEN program in MIRIAD to calculate the response of the array to a circular disk source of varying size but uniform brightness, using a synthesized beam $6''.478 \times 6''.275$. The results are shown in Figure 4, and indicate that the $\text{SO } 2_2-1_1$ source size

must exceed $21''$ diameter in order to escape detention at our limit of $0.518 \text{ Jy beam}^{-1}$. This conclusion is consistent with the single-dish maps of the higher excitation 5_5-4_4 and 6_5-5_4 transitions whose size as shown in Table 1 exceeds $40''$. The lower excitation 2_2-1_1 transition might be expected to have a source size somewhat larger. On the basis of this conclusion we will assume that no significant small-scale structure in the SO emission is missed in the single-dish results. Because the line profiles are identical for SO , CS , H_2CO , and nearly so for SiO , we

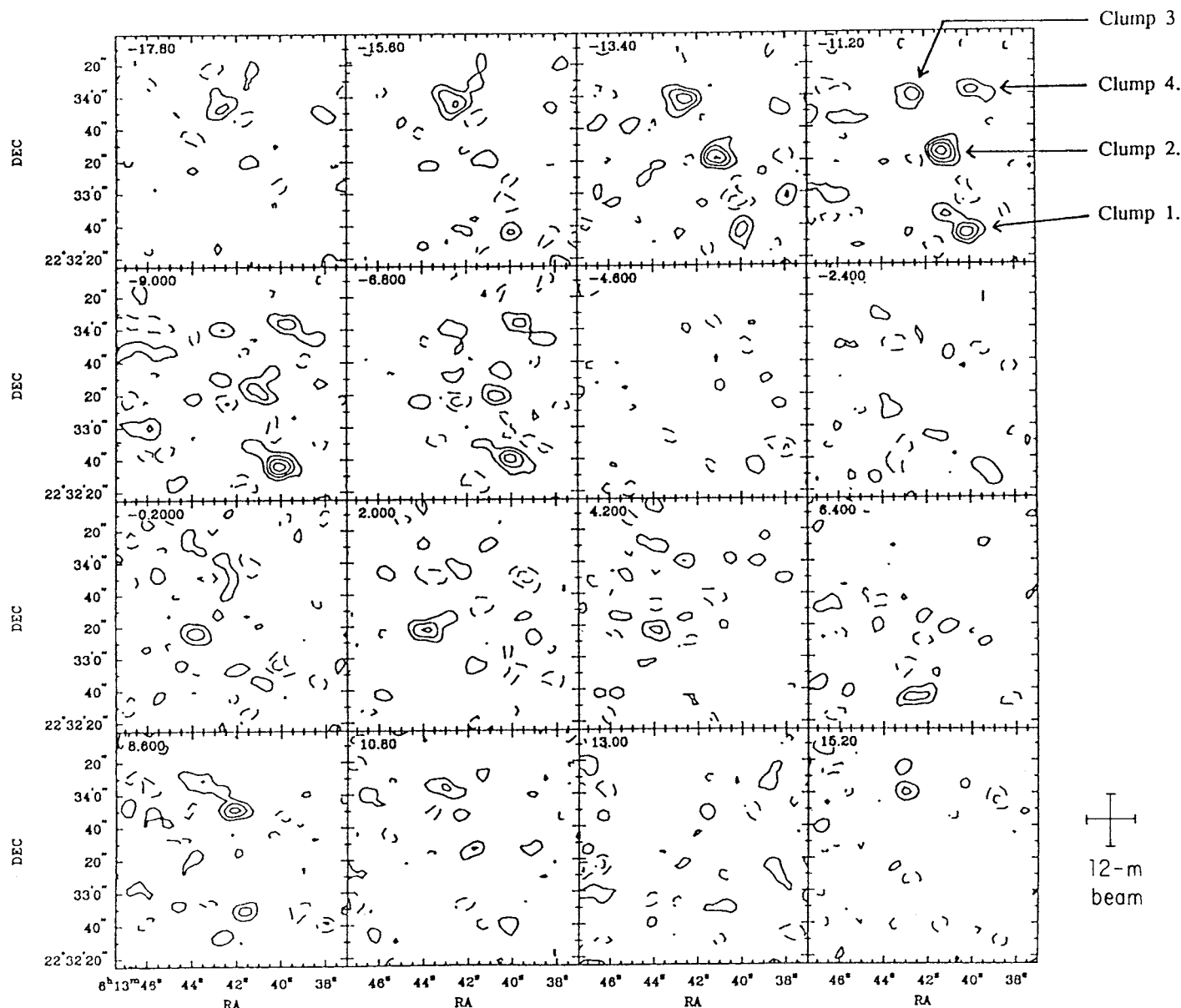


FIG. 2.—BIMA maps of HCO^+ , $J = 1-0$, with phase center at IC 443G (0, 0) position. Velocity coverage is from -17.8 to 15.2 km s^{-1} . Contour levels ($\times 0.015$) are $-80, -60, -40, -20, 20, 40, 60, 80, \dots, 220 \text{ Jy beam}^{-1}$. The BIMA beam size is $15''.4 \times 8''.3$. The 12 m telescope beam ($72''$) is shown.

shall further assume that the latter three species also contain no fine-scale structure unobserved by the 12 m telescope. This assumption has further support in that our excitation analysis (§ 3) indicates that SO (along with H_2CO) has the highest excitation density of any of the observed species. Highest densities are expected to correspond to smallest regions, so we expect no species to contain unresolved structure if SO does not. Our assumptions are not inconsistent with the fact that HCO^+ , the species with lowest excitation density (§ 3), shows small-scale structure. As we have shown, this small-scale structure is an insignificant fraction of the total single-dish flux per beam.

3. EXCITATION AND ABUNDANCE ANALYSIS

The crux of our analysis is the use of two or more transitions which have significantly differing Einstein A coefficients (transitions in the 3 and 1.3 mm region satisfy this condition

for the species under study) and hence whose intensity ratios depend sensitively on the density (but not necessarily on the temperature). The limiting factors in such an analysis are then (1) the reliability of the observed intensity ratio (limited largely by the different beam sizes used for the two transitions); (2) lack of calculated collision rates (for CN, SO); (3) the effects of electron excitation (the collision rates for which are uncertain, as is the fractional ionization of the exciting region); and (4) unknown cloud structure; we assume that constant values of n , T apply to each of regions 1 and 2 in our excitation models.

The problem of intensity ratios between the observed transitions has been partly overcome by mapping all species with $30''$ or better resolution at 1.3 mm, and by using interferometry on HCO^+ and SO, from which we argue that no significant small-scale structure exists for these or the other species at scales much less than the single-dish $30''$ resolution. The

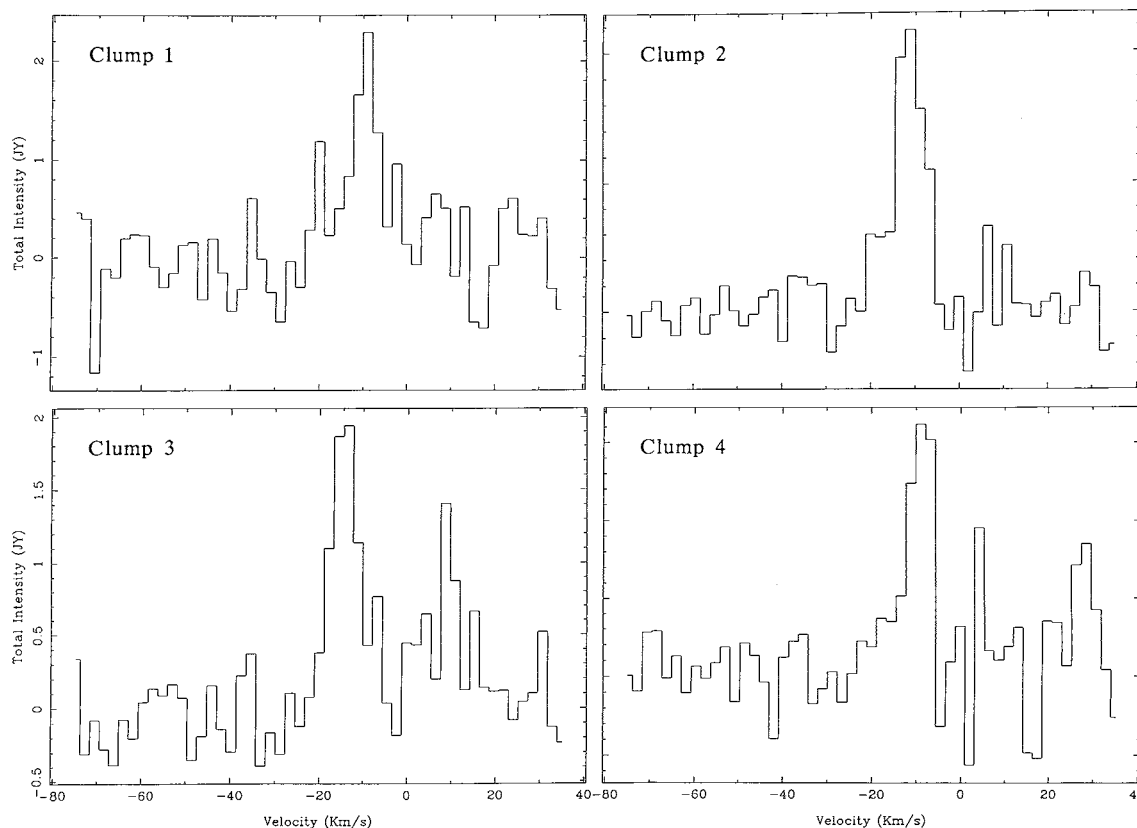


FIG. 3.—BIMA spectra for HCO^+ , $J = 1-0$, for each of the four clumps. Resolution is 0.625 MHz or 2.1 km s^{-1} .

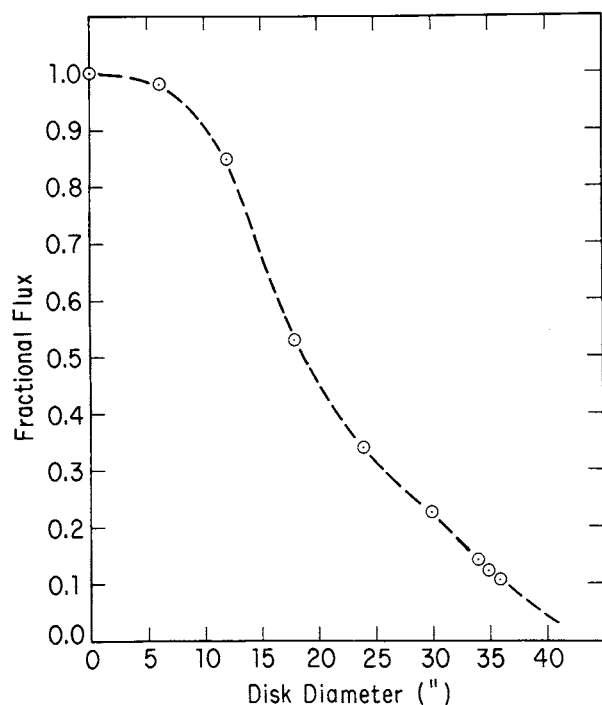


FIG. 4.—BIMA fractional response to disks of uniform brightness as a function of disk size. A comparison of the $\text{SO } 2_2-1_1$ single-dish flux with the upper limit found with the BIMA array shows that the SO emission has no angular structure smaller than $21''$.

remaining question is that of significant structure at the $30''$ – $1'$ scale, which dictates whether $T_B = T_R^*$ or T_R^*/η_c . If the latter, the value of η_c differs by a factor of ~ 2 between 1.3 and 3 mm for the 12 m telescope, so the corresponding brightness ratio between the two transitions is possibly unreliable to this degree. From the maps given in Table 1 we surmise that there is some variation of T_R^* on the $30''$ scale at 1.3 mm as well as on the $1'$ scale at 3 mm. The near sidelobes typically contain emission, so η_c is effectively near unity, but the source brightness averaged over the four cardinal points centered on (0, 0) is typically 50%–70% of the (0, 0) brightness, so there is also some beam dilution. Thus $T_B = T_R^*/\eta_c$ is a good compromise, although we justify this assumption on a case-by-case basis in what follows. The derived abundances depend little on this assumption, although densities (n) depend on it noticeably. One important conclusion, namely, that observed line widths vary inversely as n among the species, is quite safe if we make the same assumption for all species, and if they are reasonably coextensive in each of regions 1 and 2.

Our analysis considers only the central (0, 0) position, which according to our 1.3 mm maps is appropriate for HCO^+ , SiO , SO , and H_2CO but possibly less so for HCN , CN , and CS , where the peak position may be somewhat displaced.

3.1. CO

White et al. (1987) have observed $^{12}\text{CO } 1-0$ and $2-1$ and $^{13}\text{CO } 2-1$ toward IC 443G. Both transitions of ^{12}CO have $\Delta v = 35 \text{ km s}^{-1}$ (full width to zero baseline), and both show narrow ($\Delta v \approx 3 \text{ km s}^{-1}$) self-absorption at $v_{\text{LSR}} = -5 \text{ km s}^{-1}$.

The self absorbed feature is seen as emission in the ^{13}CO 2–1 line, indicating that the hot, high-velocity gas producing the wide lines lacks the excitation to produce significant background emission which the foreground absorbing cloud can absorb. If the abundance ratio $^{12}\text{CO}/^{13}\text{CO}$ is 89, the opacity of the wide ^{12}CO 2–1 line arising from IC443G is ~ 2.5 . Assuming negligible beam dilution, we find $T_B(^{12}\text{CO } 2-1) = 22$ K and $T_B(^{12}\text{CO } 1-0) = 15$ K. Thus we have three constraints in solving for the excitation conditions of CO. If we assume that most carbon is in the form of CO, then the fractional abundance $X(\text{CO}) = 1.5 \times 10^{-4}$, similar to the average over the eight ion-molecule models of Herbst & Leung (1989, hereafter HL). A value $X(\text{CO}) = 5 \times 10^{-5}$ would allow for depletion of carbon by a factor of 2.5 (cf. van Dishoeck & Black 1988). We consider X , n , and T as free parameters.

In our large velocity gradient (LVG) analysis we find $X' = X/(dv/dR) = 3 \pm 0.5 \times 10^{-7}$, $T = 33$ K, and $n = 4.4 \pm 0.3 \times 10^4 \text{ cm}^{-3}$. The line brightness ratio alone can be fitted by a variety of (n, T) values, but the opacity constrains the values of (n, T) precisely, being too low for higher T and too high for lower T . Our results differ modestly from those of White et al. (1987), who obtained $n = 8 \times 10^3 \text{ cm}^{-3}$ for an assumed $T = 50$ K. Assuming $\theta_s = 1.5$ at a distance of 1.5 kpc (Fesen & Kirshner 1980) and a line-of-sight depth equal to the projected size, we find $dv/dR = 53 \text{ km s}^{-1} \text{ pc}^{-1}$, or $X(\text{CO}) = 1.6 \times 10^{-5}$, much lower than the value 9×10^{-5} of White et al., who used only a slightly larger value of dv/dR ($75 \text{ km s}^{-1} \text{ pc}^{-1}$).

We have also analyzed the CO results with a microturbulent radiative transfer model, which requires n , T , X , and the cloud diameter L as inputs. For $L = 2 \times 10^{18} \text{ cm}$ (as above), we obtain $n = (5 \pm 0.3) \times 10^4 \text{ cm}^{-3}$, $T = 33$ K, and $X = 1.0 \times 10^{-5}$, results which are highly consistent with the LVG ones. Here the product XL is the determinable quantity (n and T are well established independently by the opacity constraint, as in the LVG model). Separating X and L in the microturbulent case is equivalent to choosing $dv/dR = \Delta v/L$ in the LVG case. It is unlikely that $X(\text{CO})$ exceeds our chosen value, but it could be less, since $\theta_s > 1.5$ is quite possible for the CO emission.

An average over the eight ion-molecule models of HL gives $X(\text{CO}) = 1.25 \times 10^{-4}$ with a range $(0.81-1.5) \times 10^{-4}$. Carbon depletion factors of 2.5 are typical of clouds with modest extinction (van Dishoeck & Black 1988) but could be much larger for the IC 443G clump, whose extinction $A_v \approx 100$ mag if uniform conditions obtain (or even larger as deduced from H_2CO and SO; see §§ 3.7 and 3.8). Our results imply a depletion factor of 10 if the shock has not modified the CO abundance. Significant increases in $X(\text{CO})$ are not expected on the basis of shock models, since none of the formation routes to CO in the recombining gas behind a dissociating or nondissociating shock contain a strong temperature dependence (Mitchell & Deveau 1983). In fact, the Neufeld & Dalgarno (1989) model of a D shock predicts a decrease by a factor of ~ 4 in $X(\text{CO})$ compared with ion-molecule chemistry (Table 4).

3.2. HCO^+

White et al. (1987) observe a peak value of $T_{\text{MB}}(1-0) = 4.5$ K with the Nobeyama $15''$ beam, while we find $T_{\text{MB}} = T_R^*/\eta_c = 3.33$ K with the 12 m $70''$ beam. Given the extended nature of the HCO^+ emission (Table 1) and the lower sensitivity of the White et al. result, we assign no significant differences to these values, and hence no dilution by the 12 m beam. G. Mitchell

(1989, private communication) observes $T_{\text{MB}}(3-2) = T_A^*/0.65 = 2.46$ K with the JCMT ($21''$ beam), and we observe $T_R^*/0.32 = 2.21$ K at the 12 m ($26''$ beam), in good agreement. Finally, White et al. observe $T_{\text{MB}}(4-3) = 1.6/\eta_b$ at the UKIRT 3.8 m telescope (beam = $54''$), where η_b is very uncertain. Line widths are $\Delta v(1-0) = 24 \text{ km s}^{-1}$ at half-intensity, but $\sim 42 \text{ km s}^{-1}$ to zero baseline; $\Delta v(3-2) = 22.4$ and 45 km s^{-1} , respectively; and $\Delta v(4-3) \sim 11 \text{ km s}^{-1}$ to zero baseline, the latter value being extremely uncertain. We use the 12 m values and ignore the $J = 4-3$ results. Both 1–0 and 3–2 profiles indicate the presence of high-velocity wings (Fig. 1).

Our HCO^+ models (LVG and microturbulent) of 1–0 and 3–2 transitions use “low-temperature” collision rates ($5 \text{ K} \leq T \leq 40 \text{ K}$, seven levels scaled from those of N_2H^+ ; see Monteiro 1985; Green 1975) and high-temperature collision rates by S. Green (1990, private communication) ($40 \text{ K} \leq T \leq 100 \text{ K}$, 11 levels). For $T > 100 \text{ K}$ the collision rates have been scaled by the factor $(T/100)^{1/2}$. An additional scaling factor of 2.0 has been applied to account for the ion charge. The results are shown in Figure 5a, in which n and T are not independently constrained because only two transitions are used, and where X is derived assuming $\theta_s = 40''$ (G. Mitchell 1990, private communication) and a line-of-sight depth equal to the projected size, hence $dv/dR = 82.8 \text{ km s}^{-1} \text{ pc}^{-1}$. For the latter, the high-velocity wing has been ignored and $\Delta v = 24 \text{ km s}^{-1}$ adopted. Regardless of the value of T , the density n is higher for HCO^+ than for CO. The discrepancy of up to 38% in X between the two models can in principle arise because of line saturation in the microturbulent model, but not in the present case, for which all transitions are always optically thin. Nor is the discrepancy due to an incorrect value of dv/dR , since both $X(\text{LVG}) = X'(dv/dR)$ and $X(\text{microturbulent}) \sim \Delta v/L$ are proportional to dv/dR . For all solutions, $T_B(4-3)$ lies in the range 0.8–1.15 K, less than the observed value (White et al. 1987) even if the beam efficiency of the UKIRT telescope is unity.

The abundance ratio HCO^+/CO ranges from 2.4×10^{-5} for lower T to 1.1×10^{-4} for higher T . The lower value is consistent with ion-molecule models having low (“depleted”) metal content (HL), while the higher values are not consistent with these or with high-metal (undepleted) models, and may indicate a shock enhancement of HCO^+ . Since $X(\text{CO})$ may be less than the adopted value of 10^{-5} , the HCO^+/CO ratio may be even higher. A D-shock model (Neufeld & Dalgarno 1989) predicts somewhat smaller abundances than ion-molecule chemistry.

3.3. HCN

White et al. (1987) observe a peak value of $T_{\text{MB}}(1-0) = 3.9$ K with the Nobeyama $17''$ beam, and we obtain $T_{\text{MB}} = T_R^*/\eta_c = 1.64$ K with the 12 m $74''$ beam. The ratio is larger in favor of the Nobeyama result than was the case for HCO^+ , suggesting significant beam dilution by the 12 m beam, even though our maps (Table 1) indicate no beam dilution. If the brightness of the 1–0 transitions is distributed similarly to that of the 3–2 transition (Table 1), then in the 12 m beam the possible peak to the west of position (0, 0) would compensate for the decrease $20''$ to the east, while the Nobeyama beam would essentially see only the (0, 0) brightness. Therefore we ignore the possibility of 12 m beam dilution. The 1–0 profile (Fig. 1b) shows the three hyperfine components, which have been Gaussian-deconvolved and the resultant intensities added to give an equivalent upsplit 1–0 intensity of $T_R^* = 1.56$ K, or $T_{\text{MB}} =$

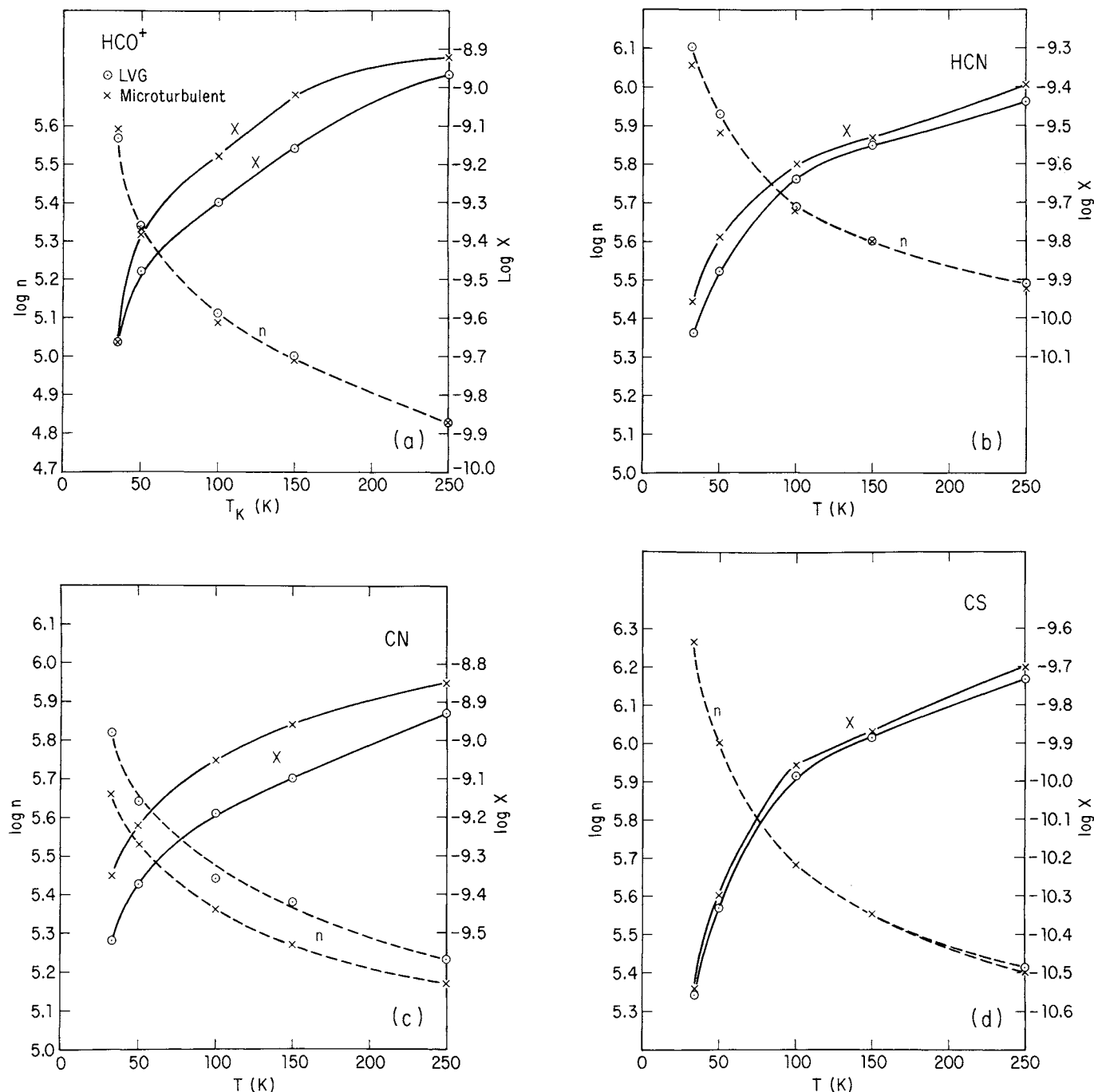


FIG. 5.—LVG and microturbulent radiative transfer solutions for (a) HCO^+ , (b) HCN, (c) CN, (d) CS (new collision rates have been calculated for CS), and (e) SiO (new collision rates have been calculated for SiO).

2.44 K. The fitted line width is 20.7 km s^{-1} . We have averaged the 3–2 intensity over the map to give $T_R^* = 0.52 \text{ K}$, or $T_{\text{MB}} = 1.51 \text{ K}$. The average differs by only 17% from the (0, 0) value. The 3–2 line width is 18.0 km s^{-1} (Fig. 1; the hfs has negligible effect for this transition). The HCN 1–0 transition exhibits the same self-absorption at -5 km s^{-1} as HCO^+ , although the fractional absorption is less. Since the excitation conditions are very similar for the two species, the abundance ratio HCN/HCO^+ is probably less than unity in the cool, foreground cloud. A ratio similar to that in the warmer “shocked” cloud ($\text{HCN}/\text{HCO}^+ \approx 0.5$) is consistent with the observations.

The LVG and microturbulent models use collision rates by Green & Chapman (1978) for eight levels and $5 \text{ K} \leq T \leq 100 \text{ K}$. Scaling by $(T/100)^{1/2}$ is used for $T > 100 \text{ K}$. The results, qualitatively similar to those of HCO^+ , are shown in Figure 5b. For all T , the derived value of n exceeds that of HCO^+ . We have adopted $\theta_s = 30''$, since comparison of the Nobeyama results with the 12 m results suggests a somewhat smaller source than for HCO^+ . Thus, for a line-of-sight depth equal to the projected size, $dv/dR = \Delta v/L = 94 \text{ km s}^{-1} \text{ pc}^{-1}$, similar to that for HCO^+ . The dependence of n on T is very similar for the two models, while that of X on T is closer than for HCO^+ .

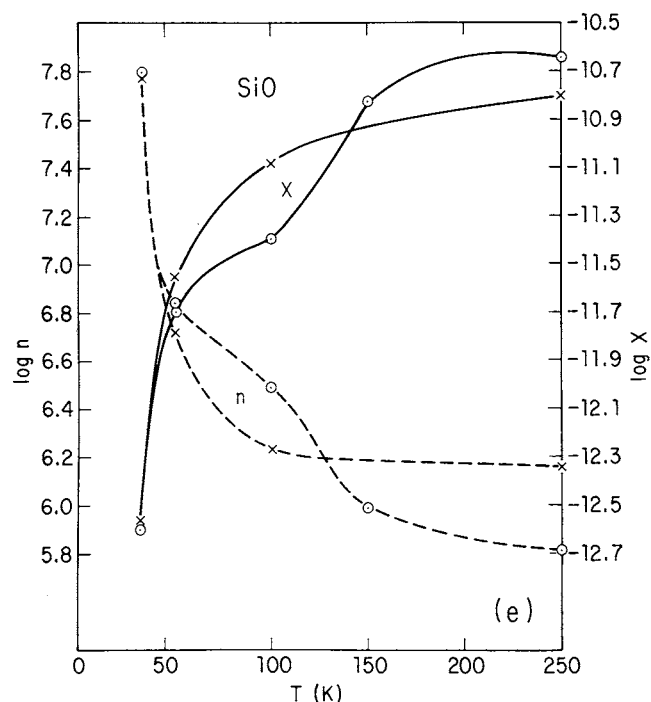


FIG. 5—Continued

The observed values for HCN/CO range from 10^{-5} for lower T to 3.8×10^{-5} for higher T . The four steady state ion-molecule models of HL give a range $(1.1\text{--}6.2) \times 10^{-5}$, consistent with observations. The four early-time models give 1.9×10^{-3} to 1.5×10^{-2} , clearly ruled out by the observations. If the warm IC 443G clump is shocked, then the shock has no dynamical or mixing effects suitable for renewing the chemistry on the size scale of the overall clump, or on the time scale since the clump was shocked ($\sim 10^4$ yr). A D shock is predicted to give an HCN abundance similar to that of ion-molecule processes (Neufeld & Dalgarno 1989; see Table 4), while ND shocks (Mitchell 1984b) predict much larger abundances.

3.4. CN

CN has a ground state $^2\Sigma^+$, and additional hfs arising from the quadrupole moment of the N atom. It may be analyzed as an equivalent $^1\Sigma^+$ species with no hfs by adding the hyperfine (hf) intensities of all hf transitions (observed or unobserved).³ For the $N = 1-0$, $J = 3/2-1/2$ multiplet, a Gaussian deconvolution of the $F = 3/2-1/2$ and $F = 5/2-3/2$ transitions has been made. The other three transitions in this multiplet are not blended, but lie on an extended high-velocity wing (Fig. 1b); an estimated “baseline” for this wing has been subtracted. In

adding the hf intensities, the sum of $J = 3/2-1/2$ hf intensities is multiplied by 1.5 to account for the total intensity in the unobserved $J = 1/2-1/2$ transition. For $N = 2-1$, $J = 5/2-3/2$, the three strong components $F = 5/2-3/2$, $F = 7/2-5/2$, $F = 3/2-1/2$ are all within 0.4 channels of each other, and the observed intensity is just their sum. The three weak transitions all lie on the high-velocity wing, and their intensities are uncertain. The sum of the three strongest transitions is multiplied by 1.122 to give the total intensity of $J = 5/2-3/2$, and then by 1.667 to give the total $N = 2-1$ intensity.

Because of the high-velocity wing, which contaminates the weaker hf components of both $N = 1-0$ and $N = 2-1$, and because of the severe blending of the stronger hf components in each case, it is difficult to estimate opacities from hf intensity ratios. In one case, the $N = 1-0$, $J = 3/2-1/2$ $F = (5/2-3/2)/F = (1/2-3/2)$ ratio, the observed intensity ratio is 9.15 while the ratio of relative intensities is 21.7, suggesting a significant opacity ($\tau \sim 3$). However, we shall find that other explanations are preferred.

The maps of both $N = 1-0$ and $N = 2-1$ transitions indicate that the 12 m main beam is essentially filled but the sidelobes are not. Thus $T_B = T_R^*/\eta_c$ is adopted in both cases, giving $T_B(1-0) = 1.86$ K, $T_B(2-1) = 1.92$ K. The latter could be slightly underestimated: Table 1 suggests that a dilution factor η_f as small as 0.7 is possible.

Collision rates for CO have been utilized to model the CN excitation, despite the large difference in dipole moments. This is because, at least for He collisions, the short-range anisotropies control the scattering, and CO and CN look electronically similar, have similar center of mass relative to nucleus positions (similar rotation constants), and have similar rotational inelasticity compared with thermal energy. For H_2 collisions, at least when H_2 is rotationally excited, the dipole interaction will enhance the $\Delta J = 1$ transitions much more for CN than for CO. At $T = 300$ K, as applies to the hottest parts of IC 443G, about half the H_2 will be rotationally excited ($J = 1$), but CN likely occurs in much cooler gas. The CO collision rates include 10 levels and temperatures up to 100 K. Scaling by $(T/100)^{1/2}$ is applied for $T > 100$ K.

Model results are plotted in Figure 5c. For all solutions, $\tau(N = 1-0)$ is found to be $\lesssim 0.05$, $\tau(N = 2-1) \approx 0.5$, while $T_{ex}(1-0) \gg T_{ex}(2-1)$. This is the well-known “bottleneck” process produced by spontaneous emission in the presence of “hard” collisions (Goldsmith 1972; Turner 1973). The effect is suppressed by increased opacity. Therefore, when hfs is considered, the weaker hf transitions will have more pronounced bottlenecks than the stronger ones, producing “anomalous” hf ratios similar to those produced by large opacity. This can explain the anomalous $F = (5/2-3/2)/F = (1/2-3/2)$ ratio described above.

Adopting a $30''$ source size (line-of-sight depth, and projected size), we find $dv/dR = 69$ km s $^{-1}$ pc $^{-1}$. There is relatively poor agreement between microturbulent and LVG models (Fig. 5c), possibly because of the strong bottleneck effect, which is more extreme in the LVG model [$\tau(N = 1-0) \approx 0.05$ for microturbulent models, ~ -0.01 for LVG models, corresponding to negative T_{ex}].

The derived abundances of CN agree quite well with steady state ion-molecule models of HL but are a factor of ~ 100 smaller than early-time predictions. The observed range of CN/HCN is 3.7 for lower T to 2.9 for higher T . The four steady state models give a range 0.4–2.3. D-shock models predict abundances similar to those of ion-molecule chemistry

³ This method is valid only if opacities are very much less than 1 for all hf transitions. An alternative method, used by Turner et al. (1990) for the $N = 1-0$ transition of CH_2CN , makes use of the fact that the Einstein A coefficients are related by $A(N = 1-0) = A(F = 5/2-3/2)$, so that if one substitutes the strongest hf intensity for the overall $N = 1-0$ intensity in a statistical equilibrium analysis, in which spin doubling and hfs are ignored, then one finds $N(N = 0) = (3/2)N(J = 1/2, F = 3/2)$, and thus a correction for the splittings can be made by applying a simple multiplicative factor. Unfortunately, although for the $N = 2-1$ transition a corresponding relation $A(N = 2-1) = A(F = 7/2-5/2)$ holds, in this case $N(N = 1) = 3N(J = 3/2, F = 5/2)$ —thus a different multiplicative factor, hence this method cannot be applied when more than one rotational transition is involved as input.

(Neufeld & Dalgarno 1989), while ND-shock models (Mitchell 1984b) predict much larger abundances (Table 4).

3.5. CS

CS is similar in spatial distribution to CN, both species peaking in intensity $\sim 30''$ south of the (0, 0) position of IC 443G. Unlike CN, CS also shows an asymmetry between the two observed transitions in the east-west sense, the 2–1 line peaking at the west position and the 5–4 line at the east position. There may be significant differences in velocity and line width of the 2–1 transition at the east and west positions, but these are not apparent in the noisier $J = 5-4$ spectra. The $J = 5-4$ intensity distribution (Table 1) indicates that the main beam is essentially filled at an intensity similar to that observed at the (0, 0) position, while the intensity falls sharply at the first sidelobes and beyond. Thus we adopt $T_B = T_R^*/\eta_c = 0.77$ K. The $J = 2-1$ emission by contrast probably fills the near sidelobes to the south and east, so that $T_B < T_R^*/\eta_c$. We have adopted a value $\eta_c(\text{eff}) = 0.81$, the average of $\eta_c = 0.62$ (for a small source) and unity. Thus $T_B(2-1) = 0.58$ K.

We have extended earlier calculations of collisional excitation rates to cover the 100–300 K range as described in the Appendix. LVG and microturbulent models give almost identical results for n and X as a function of T (Fig. 5). Again we adopt a source size (line-of-sight depth, and projected size) of $30''$, although this may be an overestimate in view of the small line widths shown by CS (Table 1; Fig. 1). Then $dv/dR = 47$ km s^{-1} pc $^{-1}$. A bottleneck effect is evident in the level populations for $T \geq 100$ K, producing very large or negative values of $T_{ex}(2-1)$ and very small or negative $J = 2-1$ opacities. The $J = 5-4$ transition is not affected and always exhibits small opacity, ~ 0.08 for all values of T .

By comparison with the (0, 0) position (Table 3), densities are higher at the east position ($\sim 8 \times 10^5$ cm $^{-3}$ at 100 K) and lower at the west position ($\sim 2 \times 10^5$ cm $^{-3}$ at 100 K), owing to the different $T_B(5-4)/T_B(2-1)$ ratios. Abundances are $\sim 3.5 \times 10^{-10}$ and $\sim 6 \times 10^{-11}$ at west and east, respectively.

Densities derived for CS are higher than for any species discussed so far (Table 3). Unlike the other species discussed so far, the observed CS abundance does not fit any of the ion-molecule models of HL. The models predict similar steady state and early-time abundances; the observed values are ~ 250 times lower than the low-metal models and $\sim 50,000$ times lower than the high-metal models. Like H_2CO and SiO, CS is very highly suppressed in IC 443G relative to most other species. Unlike the species already discussed, both CS and the species which follow are explainable in terms of an ND shock rather than a D shock (Table 4).

3.6. SiO

SiO has a spatial distribution similar to SO (Table 1) and peaks at the (0, 0) position within the uncertainties. The $J = 2-1$ emission uniformly fills the 12 m main beam and appears to fall off sharply, at least to the south, outside the main beam. Thus $T_B(2-1) = T_R^*(2-1)/\eta_c = 0.19$ K is a good estimate. The $J = 5-4$ emission does not fill the main beam uniformly, but appears to fall off well inside the beam, constituting some beam dilution. Assuming no dilution gives a minimum $T_B(5-4) \geq T_R^*/\eta_c = 0.54$ K. The best estimate for the dilution factor is $\eta_f \approx 0.6$, or $T_B(5-4) = 0.89$ K. The latter constitutes an unusually large ratio $T_B(5-4)/T_B(2-1) \approx 4.8$ but is well explained by the SiO collision rates, if $T \geq 100$ K.

We have calculated new collisional excitation rates for SiO

to cover the range 20–300 K. Details are given in the Appendix. Our new results differ importantly from those obtained by extrapolating the results of Bieniek & Green (1983) using their analytical fitting forms intended for high T . In particular, the dominance by $\Delta J = 2, 4, 6, \dots$ collisions is greatly diminished.

LVG and microturbulent models give slightly discrepant results for SiO (Fig. 5e). The results for $T \geq 100$ K involve negative T_{ex} and τ for the $J = 2-1$ transition (the bottleneck effect). Opacities are generally too low (e.g., ~ 0.02 for $J = 5-4$) to quench this behavior. The LVG approach seems particularly sensitive to this behavior. We adopt a source size of $30''$, giving $dv/dR = 65$ km s^{-1} pc $^{-1}$. As for all species, we emphasize that if the cloud size L is smaller than assumed, X will increase proportionately by the same factor in both models, while n will be essentially unaffected.

An important point is that if there is any beam dilution of the $J = 5-4$ transition, then the ratio $T_B(5-4)/T_B(2-1)$ exceeds 3, and this cannot be modeled unless $T \geq 100$ K. The observations suggest some beam dilution.

The observed abundance of SiO ranges from 10 times lower than the “standard rates” low-metal models (steady state and early-time) of HL to a factor 10^5 lower than the high-metal models. ND shocks (Hartquist et al. 1980) explain the observed abundances well.

3.7. SO

Although many transitions have been observed for SO (Table 1), an independent determination of T and n is only partly successful, since the energy level scheme is not as sensitive to T as for H_2CO (Turner & Lubowich 1991). The 12 m main beam appears fairly uniformly filled by emission from the 3 mm transitions, and thus $T_B = T_R^*/\eta_c$ is used, leading to $T_B(3_2-2_1) = 0.27$ K, $T_B(2_3-1_2) = 0.056$ K, $T_B(2_2-1_1) = 0.037$ K. At 1.3 mm, there is probably a small beam dilution, which we ignore, giving $T_B(5_5-4_4) = 0.53$ K, $T_B(6_5-5_4) = 0.92$ K. The maps show that both 1.3 mm transitions peak at the (0, 0) position, but $SO(3_2-2_1)$ possibly peaks at the west and south positions. The difference is probably not significant. All transitions are weaker to the east. Line widths at center and west are smaller than the average at both wavelength ranges. Most unusual is the fact that line widths appear larger at 1.3 mm (average 13.1 km s^{-1}) than at 3 mm (average 10.7 km s^{-1}). Since velocities are the same at 1.3 and 3 mm, this means that high-velocity gas in both blue and red wings might be highly excited. This gas is not included in our models.

Collision rates for SO are unknown. Accordingly, we have utilized five different models of collision rates varying from dipole selection rules to very “hard” collisions (see Turner 1991b for a description). Four of the five models give consistent results. If excitation by electrons is omitted then the five observed lines are best fitted by $n = (1 \pm 0.3) \times 10^7$ cm $^{-3}$, $T = 250-300$ K. If electron excitation is included, the best fit is $x_e = 2 \times 10^{-5}$ to 10^{-4} , $n = (7 \pm 1) \times 10^6$ cm $^{-3}$, $T = 250-300$ K. For all models, the 5_5-4_4 , 6_5-5_4 , and 3_2-2_1 lines are well fitted (within a few percent), but the weak transitions 2_3-1_2 and 2_2-1_1 have model values consistently ~ 2 times stronger than observed. The derived values of x_e , n , T are remarkably similar to those found by Turner & Lubowich (1991) for H_2CO , suggesting that SO and H_2CO coexist. Assuming a source diameter of $30''$ (line-of-sight depth, and projected size), we find $X(\text{SO}) = (2.4 \pm 0.4) \times 10^{-11}$.

The observed abundance of SO is a factor of 1000 smaller than the low-metal ion-molecule models (steady state or early-

TABLE 2
NEGATIVE RESULTS AND COLUMN DENSITY UPPER LIMITS

Species	Transition	Frequency (GHz)	S_{ij}	E_l (cm ⁻¹)	μ_i (debye)	T_B (mK)	$N(\text{LTE})$ (cm ⁻²)	$X(\text{LTE})^a$
OCS	9-8	109.463	9.0	14.61	0.715	<8.3	<3.1 (13)	<4.7 (-11)
SiS	5-4	90.771	5.0	6.06	1.73	<32	<2.8 (13)	<4.3 (-11)
DCN	3-2	217.238	3.0	7.25	2.99	<36	<2.0 (12)	<3.1 (-12)
SO ₂	3 ₂₂ -2 ₁₁	208.700	1.667	3.70	1.63	<23	<2.3 (14) ^b	<3.5 (-10)
H ₂ CS	6 ₀₆ -5 ₀₅	205.987	6.000	17.18	1.647	{ <44 <44	<3.3 (13) ^b	...
	6 ₁₆ -5 ₁₅	202.923	5.833	26.08			<3.7 (13) ^b	<5.0 (-11)
H ₂ CCO	11 ₁₁₁ -10 ₁₁₀	220.177	10.91	45.82	1.414	<24	<2.2 (13) ^b	<3.4 (-11)
HC ₅ N	83-82	220.932	83.0	302.2	4.33	<24	<3.2 (12)	<4.9 (-12)
C ₃ H ₂	6 ₀₆ -5 ₁₅ P } 6 ₁₆ -5 ₀₅ O }	217.822	5.45	26.82	3.3	29?	2.6 (13) ^{7c}	4.0 (-11)?
	5 ₂₄ -4 ₁₃ P	218.160	3.44	24.60	3.3	<12
	5 ₁₄ -4 ₂₃ O	217.940	3.43	23.00	3.3	<19	<2.6 (13)	<4.0 (-11)
NH ₂ CHO	9 ₄₆ -10 ₃₇	221.012	1.05	57.63	0.85	<24	<2.5 (15)	<3.8 (-9)
CH ₃ CHO	12 ₀₁₂ -11 ₀₁₁ E	226.549	11.78	42.06	2.55	<37	<8.7 (14) ^d	<1.3 (-9)
	12 ₀₁₂ -11 ₀₁₁ A	226.593	11.96	42.00	2.55	<37	<8.7 (14) ^d	<1.3 (-9)
VyCN	11 ₃₈ -11 ₂₉	223.707	5.67	26.97	1.25	<72	<1.7 (15)	...
	13 ₃₁₁ -13 ₂₁₂	226.745	6.74	34.78	1.25	<37	<7.8 (14)	<1.2 (-9)
EtCN	23 ₁₂₂ -22 ₁₂₁	206.042	22.87	77.45	1.38	<44	<4.4 (14)	<6.7 (-10)
	13 ₂₁₁ -12 ₀₁₂	223.796	0.02	23.05	1.38	<48
CH ₃ OHCO	9 ₂₇ -8 ₀₈ E	211.747	0.112	13.96	1.63	<23	<4.0 (16) ^d	<6.1 (-8)
	9 ₂₇ -8 ₀₈ A	211.811	0.042	13.94	1.63	<23

^a Assumes a 30" source diameter and $n = 10^6 \text{ cm}^{-3}$, hence $N(\text{H}_2) = 6.5 \times 10^{23} \text{ cm}^{-2}$.

^b Usual partition function divided by 2, owing to ortho-para statistics, or missing levels (SO₂).

^c For ortho transition only.

^d Usual partition function multiplied by 2 to account for one internal rotor.

times) of HL, and a factor of almost 10^6 smaller than all high-metal models. The observed abundance is explained by either ND- or D-shock models (Table 4).

3.8 H₂CO

Since the earlier H₂CO results were published (Turner & Lubowich 1991), we have obtained additional observations of the 3₀₃-2₀₂ and 3₂₂-2₂₁ transitions of para-H₂CO. The slightly revised values are $T_B(3_{03}-2_{02}) = 0.47 \text{ K}$, $T_B(3_{22}-2_{21}) = 0.16 \text{ K}$, assuming $T_B = T_R^*/\eta_c$. We have reanalyzed the results in the microturbulent mode and find a best fit to the four para- and four ortho-H₂CO observed lines of $n = 7 \times 10^6 \text{ cm}^{-3}$, $T = 300 \text{ K}$, $x_e = 10^{-3}$, $T_e = 11 \text{ K}$ if electrons are considered, and $n = 1 \times 10^6 \text{ cm}^{-3}$, $T = 200 \text{ K}$ if $x_e = 0$. Both cases now give roughly equally good fits. We find $X(\text{H}_2\text{CO}) = 2.6 \times 10^{-11}$ and 8.0×10^{-11} , respectively.⁴

Ion-molecule model abundances (HL) average 1.2×10^{-8} for steady state models and 9.2×10^{-7} for early-time models. Thus the average of the observed values is a factor of 200 below steady state predictions and 20,000 below early-time predictions. The observed value can be explained by ND shocks (Table 4).

3.9. Negative Results

Table 2 lists the results of unsuccessful searches for several molecules. Many of these (C₃H₂, OCS, SiS) have commonly been believed to be strongly enhanced in shocks, although models actually predict that OCS and C₃H₂ are greatly diminished (SiS has not been modeled). Others (HC₅N, NH₂CHO, VyCN, EtCN, CH₃OCHO) are complex species whose relationship to possible shock activity in sources such as

Orion-KL is unclear, although some are clearly enhanced in the hot Orion-KL core (e.g., VyCN, EtCN; see Turner 1991b).

We have performed a simple LTE analysis of the species listed in Table 2, assuming in each case $T = 250 \text{ K}$, $\Delta v = 12 \text{ km s}^{-1}$. Use of LTE is reasonably accurate, given the high densities derived for the detected species. To derive fractional abundances, a source diameter of 30" and a density of 10^6 cm^{-3} are adopted, corresponding to $N(\text{H}_2) = 6.5 \times 10^{23} \text{ cm}^{-2}$. Although many transitions are observed for several species listed in Table 2, the abundance is given alongside the particular transition that gives the lowest upper limit. In the case of C₃H₂, the possible detection of the blended 6-5 transitions of para and ortho species is consistent with the negative results for the 5-4 transitions.

4. TESTS OF SHOCK CHEMISTRY

4.1. Relevant Physical and Dynamical Factors

Derived densities n , fractional abundances X , and line widths Δv are summarized in Table 3. Line widths are always the same within the uncertainties for 3 and 1.3 mm transitions. There is a definite trend for Δv to decrease with increasing n , with the possible exception of CS. Taking both Δv and n into account, we divide the species into two groups: (1) low n , large Δv (CO, HCO⁺, HCN, CN), and (2) high n , small Δv (SiO, CS, SO, H₂CO). The inverse trend of Δv versus n is also apparent within each group, again with the possible exception of CS. The centroid velocity is very similar for all species. There is a possible trend for velocity to increase with increasing n within group 2.

The division into two distinct groups is somewhat arbitrary, and the results of Table 3 might also be interpreted in terms of a more smoothly varying relation between Δv and n . For instance, the density of HCN (group 1, $T \leq 100 \text{ K}$) is quite similar to that of SiO and CS (group 2, $T = 250 \text{ K}$). Further, $\Delta v(\text{SiO}) \approx \Delta v(\text{CN})$. Certainly, CO, HCO⁺, and HCN represent

⁴ Turner & Lubowich (1991) quoted 3×10^{-11} , for the $x_e \neq 0$ case; the new observations have allowed the possibility of the $x_e = 0$ model, although we still favor the $x_e \neq 0$ case, which gives a slightly better fit.

TABLE 3
EXCITATION DENSITIES AND FRACTIONAL ABUNDANCES^{a,b}

SPECIES	TEMPERATURE T					$\Delta\nu^{\circ}$ (km s ⁻¹)
	33 K	50 K	100 K	150 K	250 K	
A. Density (cm ⁻³)						
CO	5×10^4	30.0
HCO ⁺	4.2×10^5	2.4×10^5	1.9×10^5	1.2×10^5	24.0
HCN	7.7×10^5	4.8×10^5	4.0×10^5	3.0×10^5	20.6
CN	4.6×10^5	3.4×10^5	2.3×10^5	1.9×10^5	1.5×10^5	15.1
SiO	6.0×10^7	5.3×10^6	1.7×10^6	1.0×10^6	6.6×10^5	14.2
CS	1.8×10^6	1.0×10^6	4.5×10^5	3.6×10^5	2.5×10^5	10.3
SO	$7 \times 10^6{}^d$	10.7
H ₂ CO	$1\text{--}7 \times 10^6{}^d$	10.0 ^a
B. Fractional Abundances ^a						
CO	3.0×10^{-5}
HCO ⁺	2.5×10^{-10}	5.0×10^{-10}	5.5×10^{-10}	8.8×10^{-10}	...
HCN	1.6×10^{-10}	2.5×10^{-10}	2.9×10^{-10}	4.0×10^{-10}	...
CN	4.5×10^{-10}	6.1×10^{-10}	8.9×10^{-10}	1.1×10^{-9}	1.4×10^{-9}	...
SiO	2.7×10^{-13}	2.8×10^{-12}	8.5×10^{-12}	1.4×10^{-11}	2.3×10^{-11}	...
CS	2.8×10^{-11}	5.0×10^{-11}	1.1×10^{-10}	1.4×10^{-10}	2.0×10^{-10}	...
SO	$2.4 \times 10^{-11}{}^d$...
H ₂ CO	$2.6\text{--}8.0 \times 10^{-11}{}^d$...

^a All values of X are for $L = 6.6 \times 10^{17}$ cm (30" source diameter). $X \sim L^{-1}$.

^b T has been determined for CO, SO, and H₂CO by additional constraints. $T \geq 100$ K has also likely been established for SiO. See text.

^c 1.3 mm transitions. $\Delta\nu$ for 3 mm is generally very similar.

^d Best fit $T \geq 300$ K, for which n and X as listed apply.

^e Average over eight observed transitions (Turner & Lubowich 1991).

a group with both large $\Delta\nu$ and small n , while SO and H₂CO represent a different group, with both small $\Delta\nu$ and large n . CN, SiO, and CS might be considered to represent a third, intermediate group, though we regard the small $\Delta\nu$ of CS and the large n and relatively small $\Delta\nu$ of SiO as representative of group 2. Of course, most derived values of n in Table 3 are uncertain by factors of 2 because of uncertainties in T . The exceptions are CO, SO, and H₂CO for which T is well determined.

There is no apparent beam dilution in the observations of any of the species (Table 1). There is some evidence that all group 1 species are more extended spatially than group 2 species. All group 2 species have very similar distributions. CO is clearly more extended than the other species (White et al. 1987).

The path length L along the line of sight is unknown. In Table 3 we assume $L = 6.6 \times 10^{17}$ cm for most species, corresponding to a source diameter of 30". We assume 45" for CO and 40" for HCO⁺. According to our model of the IC 443G clump, described below, L is much less than 6.6×10^{17} cm for group 2 species, and probably a little less for HCN and CN as well. Thus X (which varies as $1/L$) is larger than indicated in Table 3.

4.2. Comparison of Observed and Model Abundances

4.2.1. Ion-Molecule Models

In Table 4 we compare observed column densities with column densities for the models of HL, derived by adopting values of L as described above, and the density n as found from the excitation calculations. Of course, not only n , but probably also L , differs among species, even within group 1. Thus the

comparison is not strictly valid for all species even within group 1, but it is probably quite reliable. Among group 1 species, CO, HCO⁺ and CN all fit the high-metal, steady state models well, but not early-time or low-metal models. HCN may also be consistent, although model abundances are about 10 times too high. By contrast, none of the group 2 species fit the models if L is the same for group 1 and group 2 species, the model column densities all being 1.5–2 orders of magnitude too high. Fractional abundances are best fitted if we assume that region 2 has $L = 6.6 \times 10^{15}$ cm. With this value, group 2 species also fit the low-metal models best, but SO requires early-time conditions and H₂CO requires steady state. While such a difference in metal content may be expected between regions 1 and 2, the discrepant conditions required by SO and H₂CO, the species with the most similar observed and derived conditions, cannot be explained. Further, the ion-molecule models predict that SO₂ and OCS would be easily detectable, so that the observed lower limits are decisive in arguing against ion-molecule chemistry, at least under the low density and temperature (2×10^4 cm⁻³, 10 K) modeled by HL. Slightly higher density and temperature models (5×10^4 cm⁻³, 20 K) by Langer & Graedel (1989) predict higher abundances for HCO⁺ and CN (factors of 10 and 100, respectively), indicating that the models themselves are not always sufficiently well defined to make definitive comparisons, at least for group 1 species. The two models agree, however, for CS and H₂CO (SiO and SO were not included by Langer & Graedel), so the evidence is strong that group 2 species as observed in IC 443G are not produced by ion-molecule chemistry.

It is of interest to compare the abundances derived for IC 443G with those deduced for the quiescent TMC-1 cold cloud (Irvine, Goldsmith, & Hjalmarson 1987). We find that

TABLE 4
OBSERVED AND MODEL COLUMN DENSITIES (cm^{-2})

Model Characteristics	CO	HCO ⁺	HCN	CN	SiO	CS	SO	H ₂ CO	OCS	SO ₂	C ₃ H ₂
A. Observed ^a											
...	1.65 (18)	6.9 (13)	7.6 (13)	1.4 (14)	1.0 (13)	3.3 (13)	1.1 (14)	7.9 (13)	<3.1 (13)	2.3 (14)	<2.6 (13)
B. Ion-Molecule Models of Herbst & Leung 1989											
$n_0 = 2 \times 10^4 \text{ cm}^{-3}$, $T = 10 \text{ K}$:											
Steady state, high-metal, $L = 6.6 (17)$	4 (18)	9.9 (13)	1.8 (15)	4.4 (14)
Steady state, low-metal, $L = 6.6 (15)^b$	3.1 (12)	4.0 (13)	1.1 (14)	1.3 (14)	>4 (14) ^c	>2 (14) ^c	>7 (11) ^c
C. Nondissociative Shock Models of Mitchell 1984a, b ^a											
$n_0 = 10^4$, $8 \text{ km s}^{-1} \leq v_s \leq 15 \text{ km s}^{-1}$	4.5 (17)	...	~3 (16)	1-6 (16)	...	1.2 (13)	3.0 (14)	0.6-10 (15)	2 (12)
D. Nondissociative Shock Model of Hartquist et al. 1980 ^c											
$n_0 = 10^6$, $v_s = 8 \text{ km s}^{-1}$	7.0 (12)	5.0 (12)	1.1 (14)	...	3.4 (13)	7.9 (9)	...
E. Dissociative Shock Models of Neufeld & Dalgarno 1989											
$n_0 = 10^5$, $v_s = 60$	4.6 (17)	5.6 (12)	5.0 (14)	1.9 (14)	1.8 (16)	...	2.3 (13)	9.8 (6)	...	9.8 (9)	9.8 (5)
$n_0 = 10^6$, $v_s = 60$	1.5 (18)	1.8 (13)	8.2 (15)	8.2 (14)	7.8 (16)	...	8.6 (14)	9.6 (6)	...	4.6 (12)	3.8 (6)
$n_0 = 10^6$, $v_s = 100$	1.7 (18)	...	2.7 (13)	1.1 (13)	1.0 (16)	...	6.1 (13)	2.4 (11)	...

^a $T = 150 \text{ K}$ for HCO⁺, HCN, CN; $T = 250 \text{ K}$ for SiO, CS, SO, H₂CO; LTE for SO₂, C₃H₂.

^b $N = nXL$ is dependent only on XL ; L is chosen to match model values of X .

^c Adopting $n = 8 \times 10^5 \text{ cm}^{-3}$. Lowest possible predictions are also adopted for these species. Hence ">"

^d SO, CS from Mitchell 1984a. CO, HCN, CN, H₂CO, C₃H₂ from Mitchell 1984b. We have multiplied model column densities of Mitchell 1984b by 3.5, so that $N(\text{H}_2) = 3.5 (21) \text{ cm}^{-2}$ applies to both models.

^e Normalized to observed $N(\text{SO})$, for which $L = 4.2 (14) \text{ cm}$.

abundances of all group 1 species in IC 443G are between 0.01 and 0.04 times the TMC-1 abundances. If the common belief is correct that species such as HCO^+ , HCN , and CN are produced by ion-molecule processes in cold quiescent clouds, then such processes cannot be dominant for these species in IC 443G. Group 2 species, by contrast, have abundances in IC 443G which are all within a factor of 4 of those seen in TMC-1, except for SiO , which is at least 500 times more abundant fractionally in IC 443G. Special considerations involving the highly refractory nature of SiO explain its unique properties (Turner 1991a), while similarities of the other group 2 species in TMC-1 and IC 443G may imply that they are not controlled by ion-molecule processes in TMC-1.

4.2.2. Shock Models

Because L is uncertain for group 2 species, we compare observed and model abundances in terms of column densities $N = XnL$, which are independent of L because $XL = \text{constant}$. The derived values of N use values of n and X as given in Table 3, and $L = 6.6 \times 10^{17}$ cm. The results are given in Tables 4C, 4D, and 4E.

We compare the observations with nondissociative (ND) shock models of Hartquist et al. (1980) and Mitchell (1984a, b) and the dissociative (D) shock model of Neufeld & Dalgarno (1989). As seen in Table 4, these models currently span a very limited region of parameter space, so that a meaningful comparison may be questioned. However, where there is overlap in modeled species under different physical conditions (Hartquist et al. versus Mitchell), agreement is good.

We may summarize the models capable of explaining the observations of IC 443G as follows: CO (D shock); HCO^+ (D shock); HCN (D shock); CN (D shock); SiO (ND shock); CS (ND shock); SO (D or ND shock); H_2CO (possibly ND shock). Thus groups 1 and 2 species again separate cleanly, group 1 requiring D shocks, group 2 requiring ND shocks. We noted that group 1 species are also explainable by ion-molecule reactions, while group 2 species are not. However, the quiescent conditions of the ion-molecule models cannot, of course, explain the large line widths observed. The present observations do show, however, that abundances of the group 1 species in a shocked region do not differ appreciably from those expected for ion-molecule chemistry, contrary to the conclusions of several earlier studies.

Some qualifications of our conclusions are in order: (1) Shock models depend importantly on n_0 (preshocked density), v_s (shock velocity), and presumably on $N(\text{H}_2)$. Some species (e.g., CN) depend critically on v_s . The model column densities for the ND models have been averaged over the range $8 \text{ km s}^{-1} \leq v_s \leq 15 \text{ km s}^{-1}$ in Table 4. (2) All models ignore magnetic fields and are for J -type shocks. Since the velocity, density, and temperature structure of C -type (MHD) shocks is much smoother (cf. Draine et al. 1983), the chemistry may differ significantly. (3) For $n_0 = 10^4 \text{ cm}^{-3}$, the dividing line for v_s between D and ND shocks is given as 17.5 km s^{-1} by Mitchell (1984a, b), but as $\geq 24 \text{ km s}^{-1}$ by others (Kwan 1977; London, McCray, & Chu 1977; Hollenbach & McKee 1980). While all current chemistry models for ND shocks use v_s well below 17.5 km s^{-1} , such discrepancies suggest the high uncertainties in shock models even for $B = 0$. (4) Hartquist et al. give only fractional abundances. To convert to column densities, we have normalized to the observed value of $N(\text{SO})$, so the comparison of model with observation actually only involves the ratio $\text{SiO}/\text{SO}/\text{CS}$, but this agrees well with observations and with the models of Mitchell.

4.2.3. A Model of IC 443G

The several well-studied molecular clumps apparently impacted by the supernova remnant (SNR) IC 443 all lie in the eastern part of the optical image, where the remnant appears to be interacting with the densest region of the ISM. Clump G is the westernmost of these, and is essentially centered on the optical image of IC 443 (Huang, Dickman, & Snell 1986). A large loop of $2 \mu\text{m}$ emission from the vibrationally excited $v = 1-0$ $S(1)$ transition of H_2 is observed beginning along the eastern edge of the SNR, arcing south and then north again, and passing through clump G at the northwest extreme of the loop (Burton et al. 1989). Clumps C and G are the brightest regions in the H_2 lines. The $[\text{O I}] \ ^3P_1-^3P_2$ line at $63 \mu\text{m}$ has also been observed at several points around clump C, and shown to contribute at least half of the flux of the $\text{IRAS } 60 \mu\text{m}$ band, which traces the same loop as the $1-0$ $S(1)$ H_2 emission (Burton et al. 1990). (The $[\text{O I}]$ line has not been searched toward clump G.) These observations prove the existence of shocks throughout the region of the clumps (X-rays and UV excitation can be ruled out), and Burton et al. model the $[\text{O I}]$ and $1-0$ $S(1)$ H_2 emission using a variety of C and J shocks. C shocks with $v_s = 10-45 \text{ km s}^{-1}$ are required, the lower velocity ones providing the $[\text{O I}]$ excitation and the higher velocity ones the H_2 excitation. These results cannot explain the nearly constant ratio of $[\text{O I}]$ to H_2 $1-0$ $S(1)$ and H_2 $1-0$ $S(1)$ to $2-1$ $S(1)$ emission over the observed positions, but a partially dissociative J shock with $v_s \sim 10-20 \text{ km s}^{-1}$ can, with the further ad hoc assumption that the O chemistry is suppressed, so that H_2O and OH are inefficiently formed. Clearly the shocked environment of IC 443 is exceedingly complex.

Clump G appears to have a simpler geometry than other observed regions. Because it is centered on the optical image, we may imagine that the shock is traveling along the observer's line of sight (los) and is striking the clump on its rear side and perhaps accelerating it toward the observer. As pointed out by Turner & Lubowich (1991), a simple planar, nonmagnetic shock is probably inappropriate, because it would impart a postshock velocity $v_c = v_s(1 - T/4T_s)$, where T_s ($\approx 10^5$ K) is the gas temperature just behind the shock when $v_s = 65-100 \text{ km s}^{-1}$ (Fesen & Kirshner 1980). Thus $v_c \approx v_s$, so that the value of v_{LSR} for IC 443G, -10 km s^{-1} , means that the preshock systemic velocity must have been $v_{\text{sys}} = v_{\text{LSR}} + v_c \approx 50 \text{ km s}^{-1}$, an unlikely velocity for material at the Galactic position of IC 443 ($l = 189^\circ$, $b = 3^\circ$). A C -type shock in which the hydrodynamic variables vary "continuously" from preshock to postshock values, allows gas to assume velocities over the entire range, $\Delta v \approx \frac{1}{4}v_s \approx 20 \text{ km s}^{-1}$ in the present case, and $v_c \sim \frac{1}{2}v_s$, thus reducing the v_{sys} problem.

The boundary conditions imposed by our observations on any model of the IC 443G clump are as follows:

1. The angular size of the high-density region 2 is essentially the same size as that of the lower density region 1. This is indicated by the single-dish maps (Table 1) and verified by the BIMA results for SO . SO (along with H_2CO) requires the highest density of any observed species, so it is reasonable to expect that other group 2 species would not have smaller structure. Thus a slab geometry, with n varying along the los but not transverse to it, is indicated. Such a geometry is consistent with a shock moving along the los in the case of clump G.

2. Observations of H I at 21 cm (Braun & Strom 1986, Fig. 1b) show a peak in T_b of $10-13 \text{ K}$ and $v_{\text{LSR}} = -10$ to -14 km s^{-1} at clump G. The presence of H I shows that some disso-

ciation of H_2 has occurred. We find $N(\text{H I}) = 1.823 \times 10^{18} \int T_B dv = 5.5 \times 10^{20} \text{ cm}^{-2}$. We also find $N(\text{CO}) = 1.65 \times 10^{18} \text{ cm}^{-2}$; hence, if $X(\text{CO}) = 5 \times 10^{-5}$, then $N(\text{H}_2) = 3.3 \times 10^{22} \text{ cm}^{-2}$. Thus $\text{H I}/\text{H}_2 = 0.017$. At $n \gtrsim 10^5 \text{ cm}^{-3}$, the recombination time is very fast ($\sim 1 \text{ yr}$), so the degree of ionization in clump G is very small. The small degree of dissociation in clump G means either that the shock is only weakly dissociating or that it failed to penetrate very far into clump G (the recombination time for $\text{H I} \rightarrow \text{H}_2$ on grains is long compared with other relevant time scales).

3. The lower n region 1 and higher n region 2 must exist before the shock, for two reasons. First, the dependence of group 1 species on density suggests that within region 1 the density increases slowly inward from the rear edge. A slow increase would be unlikely to result from a D shock impacting on this side of the clump. Second, according to the molecular abundances, a ND shock is appropriate for region 2. Such a shock would not likely produce a larger compression than a D shock.

4. The velocities of regions 1 and 2 along the los must be essentially identical.

Several possible models of clump G are suggested in Figure 6. Consider first the geometry shown in Figure 6a. Here the clump is fully embedded in hot blast-wave gas, which has swept up a shell of material that lies between the observer and the clump. Region 2, on the rear side, is subjected to a ND shock. Region 1, on the front side, is subjected to a D shock, which may approach from the side (having earlier been deflected), or essentially front-on as a result of reflection off the accreted shell. This picture has obvious difficulties. If a D shock impinges on region 1, it is difficult to explain the observed low temperatures despite a short cooling time ($< 100 \text{ yr}$ at $n_0 = 10^5 \text{ cm}^{-3}$), because high-velocity shocking material would be expected to impact region 1 over a considerable period of time, since the blast wave is locally contained by the swept-up shell of material. Thus a high temperature would be maintained. Alternatively, if ion-molecule chemistry rather than a D shock produces the observed abundances in region 1, then there is no explanation for the large line widths found in region 1.

An alternative picture is that of Figure 6b. Here region 2 is nearest the observer, and there is no swept-up material containing the blast wave. A single D shock hits the far side of the clump, producing large values of Δv and the requisite abundances, then slows during passage through the clump, becoming a ND shock by the time it reaches region 2. For $n \sim 10^5 \text{ cm}^{-3}$ in region 1, the cooling time due to radiation of H_2 ($\lesssim 100 \text{ yr}$) is much less than the time for the shock to traverse the clump ($\sim 10^4 \text{ yr}$ at a mean velocity of 15 km s^{-1} within the clump). Thus the low temperatures ($\lesssim 50 \text{ K}$) found for CO in region 1 are understandable. The $\sim 300 \text{ K}$ temperature in

region 2 is harder to explain. Since cooling times are even shorter here, the shock must have passed through this region a very short time ago. Alternatively, an elevated temperature of $\sim 300 \text{ K}$ in the thin layer of region 2 might result from thermal conduction of the hot blast-wave gas which has overtaken the clump.

The case in Figure 6b requires a rather contrived explanation of the dependence of Δv on n . According to Fesen & Kirshner (1980), the velocity v_c of a uniform density gas behind an adiabatic J-type shock of velocity v_s is given by $v_c = v_s(1 - T/4T_s)$, so that, as seen in a direction z along the shock, the line widths will be $\Delta v \sim \frac{1}{4}v_s$. Thus observed values of Δv in region 1 are explained by $v_s \sim 80\text{--}90 \text{ km s}^{-1}$, consistent with values of v_s discussed for IC 443 by Fesen & Kirshner. Further, a smaller Δv for region 2 follows naturally, because of its much smaller linear extent. However, the centroid velocities of the various molecular species in region 1 should differ on this picture, unless all region 1 species are coextensive. Thus, to maintain identical velocities as observed, all region 1 species would have to have the same Δv and hence the same n , contrary to observations. A much more complicated distribution of v_c is needed to produce a constant velocity among species but line widths differing with n as observed. Equally important, v_c reaches its maximum value at largest z , i.e., in region 2, so if the shock is of D type in region 1, it would remain so in region 2.

More realistic profiles of v_c for C-type shocks in uniform media have been constructed by Draine, Roberge, & Dalgarno (1983), using appropriate values of B for dense clouds. For these, v_c starts at zero just behind the shock and increases smoothly and monotonically to values approaching v_s (25 km s^{-1} in the models) at a distance z varying from $2 \times 10^{16} \text{ cm}$ for preshock density $n_0 = 100 \text{ cm}^{-3}$ to $8 \times 10^{16} \text{ cm}$ for $n_0 = 10^6 \text{ cm}^{-3}$. Like the simple linear function of Fesen & Kirshner (1980) for $v_c(z)$, these v_c distributions imply a variation of centroid velocity with differing line widths, contrary to observation. Again, a more complex $v_c(z)$ distribution is needed. Models with $dn/dz \neq 0$ have apparently not been constructed.

To obtain a constant centroid velocity along with differing Δv among different species, we require that v_c be essentially symmetrical about some value of z at which v_c has a maximum (see Fig. 7). Then different species occupying different regions on either or both sides of the maximum would have the same

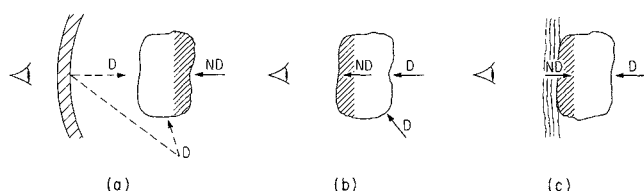


FIG. 6.—Possible geometries (schematic) of the IC 443G clump. The shaded area represents the higher density region (region 2; nondissociative shock), and the nonshaded area represents the lower density region 1 (dissociative shock).

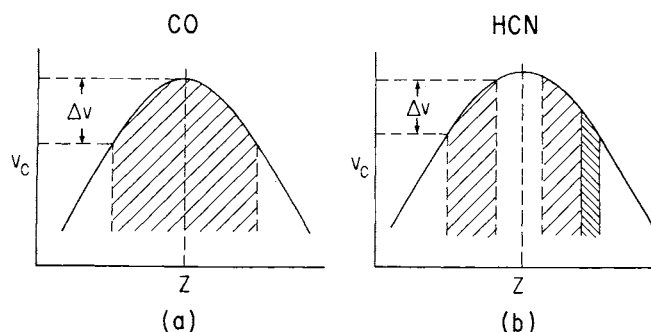


FIG. 7.—Cloud shock velocity profile and its relation to observed line widths and centroid velocities. The $v_c(z)$ curve is symmetric or nearly so about a central value of z . Then a species such as CO, produced at all shock velocities v_c , would have the same centroid velocity as a species such as HCN, produced over a more restricted range of v_c . Even a group 2 species (SiO , CS , SO , H_2CO), which we model to exist in a small, dense region of z (narrow hatched area at far right), would have the same centroid velocity, but much smaller Δv , as required by the observations. To produce such a $v_c(z)$ curve, $dn/dz \approx 0$ for z smaller than the median value, and $dn/dz > 0$ for larger z .

central velocity but line widths dependent on the range of z they occupy. Thus CO, assumed to occupy the entire region 1, would have the largest Δv . The abundance of a given species can be imagined to depend on both v_c (cf. models of Mitchell 1984a, b) and n . On this picture, the high-velocity blue wings of HCO^+ and CN (both of which lie within the CO profile) would arise from the region of z corresponding to the highest value of v_c . Evidently CO, HCO^+ , and CN can form at higher shock velocities than other species, although the abundances of HCO^+ and CN are apparently lower at the higher velocities than at lower velocities. Some asymmetry can certainly be tolerated in the $v_c(z)$ distribution without creating shifts in the centroid velocities larger than the observational uncertainties.

One further scenario can be imagined. In the picture just discussed, the preshocked clump would already contain the high- n region 2 and lower n region 1, since the shock is weaker at region 2 and the resultant compression therefore less. To avoid the requirement of such an ad hoc initial density distribution, we note that as a shock hits a clump, the momentum of the flow both moves the clump and drives a shock wave into it. Flowing interclump gas piles up at the clump boundary owing to the inertia of the accelerated clump, and thus a shock wave is sent back into the incoming flow (Silk & Solinger 1973) (see Fig. 6c). In this case the high density of region 2 could be a direct result of the piling up of preshock material, so that the preshocked clump G would consist of only a single region with the properties of region 1 ($n_0 \sim 10^5 \text{ cm}^{-3}$). This picture fails, however, because the velocity of the reverse shock, required to be 10–12 km s^{-1} to explain the line widths of region 2, would produce a corresponding shift of +10–12 km s^{-1} in the center velocities of region 2 species relative to region 1 species, contrary to observation. In addition, the foreground cold cloud giving rise to narrow absorption in the 1–0 transitions of CO and HCO^+ has systemic velocity -5 km s^{-1} . If this is also the preshock velocity of clump G, then the D shock has only accelerated the clump to $\sim -7 \text{ km s}^{-1}$, so the reverse shock has $v_s \approx 2 \text{ km s}^{-1}$, insufficient to explain the line widths in region 2.

5. CONCLUSIONS AND FUTURE PROSPECTS

We have studied eight molecular species, many of them in common with an earlier study by Ziurys et al. (1989a), in the hot dense clump IC 443G, believed to be impacted by the shock wave from the SNR IC 443. We confirm the earlier conclusion that clump G is hot and dense, but by emphasizing multiple transition observations we derive considerably different abundances in some cases, and require a much hotter ($T \geq 250 \text{ K}$), denser ($n \geq 10^6 \text{ cm}^{-3}$) clump to explain our results. The clump appears to consist of two distinct regions, one relatively cool ($T \sim 33\text{--}100 \text{ K}$, $n \sim 3 \times 10^5 \text{ cm}^{-3}$) and one hotter and denser ($T > 250 \text{ K}$, $n \gtrsim 10^6 \text{ cm}^{-3}$). Region 1 ($L \sim 6.6 \times 10^{17} \text{ cm}$) contains CO, HCO^+ , HCN, and CN, whose abundances may be explained either by ion-molecule chemistry, assuming steady state and high-metal conditions, or by a D shock of $v_s \approx 60\text{--}90 \text{ km s}^{-1}$, passing through a preshock clump of $n_0 \sim 10^5 \text{ cm}^{-3}$. Only the D-shock model can explain the large observed line widths. Region 2 gives rise to SiO, CS, SO, and H_2CO and requires a ND shock ($v_s \approx 5\text{--}15 \text{ km s}^{-1}$) passing through a region of $n_0 \approx 10^6 \text{ cm}^{-3}$. L and X are a priori uncertain for region 2, so comparisons of observations with models are made in terms of column densities. Observed fractional abundances fit ND shock models if $L \approx 6.6 \times 10^{15} \text{ cm}$. Ion-molecule chemistry is ruled out for H_2CO but not for

other group 2 species if they occupy the smaller path length. The large line widths are, however, not consistent with ion-molecule chemistry in the usual quiescent-cloud conditions. Also, the time scale for establishing even early-time ion-molecule abundances is $\geq 10^5 \text{ yr}$, much longer than the time since the shock impacted clump IC 443G.

Not only the abundances are related to the densities. The line widths bear a roughly inverse relation to the derived excitation densities, for both regions 1 and 2 and within each region. Yet all species have the same centroid velocity. These factors are explained in terms of a shock-induced gas velocity within the clump, v_c , which is a fairly symmetrical function of path length z , with maximum value somewhere in region 1. This single function includes both regions 1 and 2, indicating that there is no sharp boundary between the regions, a conclusion consistent with the derived excitation densities. In region 1 the $v_c(z)$ profile is consistent with a C-type, not a J-type, shock, which impinges on the clump face opposite the observer and proceeds approximately along the observer's los. A reverse shock entering the near face in the opposite direction (as would arise if the accelerated clump piled up mass in front of it) can be ruled out, since it would produce a difference in velocities in regions 1 and 2 which is not observed.

Our basic picture might be tested by observations of other clumps in IC 443 (clumps C, D, or E; see Huang et al. 1986), which lie in projection closer to the rim of the SNR. Any high- n "region 2" with L as small as implied for clump G would then be severely beam-diluted, so the group 2 species (SiO, CS, SO, H_2CO) would appear very weak, whereas group 1 species (CO, HCO^+ , HCN, CN) would not. Ziurys et al. (1989a) observed clump B as well as clump G, but unfortunately clump B has an aspect angle similar to that of clump G. It may be of interest that the 3 mm transitions of SiO and CS (but not SO) appear weaker in clump B than in clump G (H_2CO has not been observed in clumps other than clump G).

Our group 2 abundances are strongly dependent on the assumption of no beam dilution by the 30" observing beam. We have verified this by interferometer maps of SO; similar maps of SiO, CS, and H_2CO should be made. Similarly, our HCO^+ BIMA maps suggest no beam dilution for group 1 species (a safer assumption than for group 2), but interferometric maps would again be useful, especially to refine the rather crude relation $T_B = T_R^*/\eta_c$ which we have generally adopted. Derived abundances will not be much affected by changes in the ratio of T_B between 3 mm and 1.3 mm transitions, but densities will be significantly affected. Thus the basic conclusions about the nature of the shocks affecting each species should not change, but the details regarding the $v_c(z)$ and $n(z)$ relations are subject to revision.

All shock models to date (J type or C type, D or ND) assume a constant-density medium, whereas the interstellar gas is, of course, inhomogeneous. The speed of a shock driven into a clump of gas varies with n , and in addition the shock will be refracted if it is moving through a medium of changing n . Hence, as Mitchell (1984b) has remarked, "A given los through a shocked inhomogeneous medium may encounter a range of shock speeds and shock directions, complicating the interpretation of observed column abundances." The shock speed $v_c(z)$ affects not only abundances but also emergent Δv 's. More detailed shock models, with $dn/dz \neq 0$, are needed to test the simple picture we have proposed here. Such models are also needed to test the possibility that a C-type shock can also be dissociating, as we require in region 1.

According to our picture of IC 443G, both ND- and D-shock models, as they currently exist, seem to explain the observed abundances of the eight species we have studied in detail, as well as several other species for which we have only upper limits. This is in contrast to the Orion-KL object, for which observed abundances are in several cases in sharp disagreement with both ND- and D-shock models (e.g., the SO_2/SO ratio, the SiO and H_2CO abundances).

We thank Stu Vogel for his help and encouragement throughout this project, and for invaluable advice on the BIMA interferometric observations. We are grateful to Peter Teuben for valuable assistance in BIMA data reduction. This work was partially supported by grant AST-9100306 to the University of Maryland from the National Science Foundation.

APPENDIX

Green & Chapman (1978) presented CS- H_2 collisional excitation rates among the lowest 13 rotational levels ($J = 0-12$) of CS for kinetic temperatures up to 100 K. The most likely source of error in that study is the interaction potential for CS- H_2 , which was adapted from an electron gas model for the CS-He interaction. A system for which the electron gas model was compared with a more accurate interaction potential is CO-He, for which excitation rates were also computed from an accurate interaction obtained by solving the electronic Schrödinger equation (Thomas, Kraemer, & Dierksen 1980). The electron gas model was found to give a reasonable estimate for the total excitation rate out of a given rotational level but to err by as much as a factor of 2-3 for some individual state-to-state rates. As an additional approximation, Green & Chapman (1978) averaged the CS- H_2 interaction over H_2 orientations, which is equivalent to forcing the H_2 to remain in its lowest, $J = 0$, rotational level; this approximation becomes less valid at higher temperatures. Collisions with rotationally excited H_2 are expected to enhance $\Delta J = 1$ rates by a factor of 2-3 (Green 1977a) owing to the effect of the long-range dipole-quadrupole interaction.

It is possible with current capabilities to relax these approximations for CS- H_2 collisions, albeit at considerable computational expense. However, the methods used previously are believed to give a reasonable approximation to the collision rates and are expected to be generally adequate for analysis of the astrophysical data. Unfortunately, the earlier work did not include enough rotational levels or extend to high enough temperature to address the current observations. Therefore, the earlier study has been extended, using the same theoretical methods, to include rotational levels through $J = 20$ and temperatures to $T = 300$ K. Molecular scattering calculations used the coupled states approximation, which was found previously to be accurate to about 20% for individual cross sections. Calculations were done for a large number of energies up to about 1800 K and included as many as 36 rotational levels to ensure convergence of cross sections. Rate constants for kinetic temperatures between 20 and 300 K were obtained by averaging over thermal distributions of collision energies; these agreed well with earlier values in the region of overlap.

Collisional excitation of SiO has been considered previously by Bieniek & Green (1983). However, that study concentrated on pumping mechanisms for circumstellar masers and hence considered kinetic temperatures in the range 1000-3000 K and emphasized the relative rates of vibrational and pure rotational excitation. That study also used an electron gas model to obtain the interaction potential. Because dependence of the interaction on the SiO vibrational coordinate as well as on collision distance and orientation were calculated (Bieniek & Green 1981), only nine orientations were considered to keep the number of points manageable. This may be inadequate to describe such an anisotropic surface; it should be compared with the 11 orientations considered the

TABLE 5
CS- H_2 RATES AT $T = 250$ K

JF	JI							
	0	1	2	3	4	5	6	7
0.....	...	2.57E-11	3.74E-11	5.80E-11	6.67E-12	1.52E-12	2.61E-12	8.99E-13
1.....	7.63E-11	...	4.09E-11	5.90E-11	1.01E-11	1.33E-11	3.53E-12	5.27E-12
2.....	1.82E-10	6.69E-11	...	4.36E-11	6.64E-11	1.24E-11	1.60E-11	5.37E-12
3.....	3.84E-11	1.31E-10	5.93E-11	...	4.54E-11	6.87E-11	1.45E-11	1.76E-11
4.....	5.47E-11	2.80E-11	1.12E-10	5.62E-11	...	4.62E-11	7.03E-11	1.53E-11
5.....	1.45E-11	4.28E-11	2.44E-11	9.92E-11	5.38E-11	...	4.66E-11	7.16E-11
6.....	2.79E-11	1.27E-11	3.51E-11	2.34E-11	9.15E-11	5.20E-11	...	4.65E-11
7.....	1.04E-11	2.04E-11	1.27E-11	3.07E-11	2.15E-11	8.63E-11	5.03E-11	...
8.....	1.18E-11	1.07E-11	1.68E-11	1.13E-11	2.80E-11	2.02E-11	8.24E-11	4.94E-11
9.....	1.09E-11	9.13E-12	9.05E-12	1.47E-11	1.02E-11	2.59E-11	1.88E-11	7.95E-11
10.....	6.18E-12	8.43E-12	7.76E-12	7.79E-12	1.31E-11	9.26E-12	2.44E-11	1.78E-11
11.....	5.93E-12	5.13E-12	6.85E-12	6.70E-12	6.78E-12	1.20E-11	8.60E-12	2.32E-11
12.....	4.02E-12	4.63E-12	4.20E-12	5.70E-12	5.92E-12	5.93E-12	1.10E-11	7.98E-12
13.....	3.25E-12	3.09E-12	3.69E-12	3.51E-12	4.81E-12	5.26E-12	5.28E-12	1.01E-11
14.....	2.19E-12	2.48E-12	2.49E-12	3.04E-12	3.01E-12	4.20E-12	4.84E-12	4.84E-12
15.....	1.73E-12	1.71E-12	1.94E-12	2.05E-12	2.58E-12	2.65E-12	3.72E-12	4.50E-12
16.....	1.22E-12	1.27E-12	1.34E-12	1.56E-12	1.70E-12	2.21E-12	2.32E-12	3.28E-12
17.....	8.53E-13	9.08E-13	9.83E-13	1.07E-12	1.29E-12	1.44E-12	1.91E-12	2.07E-12
18.....	6.22E-13	6.30E-13	6.91E-13	7.79E-13	8.74E-13	1.08E-12	1.25E-12	1.69E-12
19.....	4.20E-13	4.44E-13	4.75E-13	5.38E-13	6.30E-13	7.30E-13	9.29E-13	1.09E-12
20.....	2.85E-13	2.99E-13	3.28E-13	3.66E-13	4.30E-13	5.19E-13	6.19E-13	8.04E-13

NOTE.—JF = final J ; JI = initial J .

TABLE 6
SiO-H₂ RATES AT $T = 250$ K

JF	JI							
	0	1	2	3	4	5	6	7
0.....	...	1.26E - 11	5.56E - 11	3.39E - 12	1.37E - 11	1.17E - 12	5.45E - 12	1.11E - 12
1.....	3.74E - 11	...	2.13E - 11	9.43E - 11	6.33E - 12	2.77E - 11	3.37E - 12	1.06E - 11
2.....	2.71E - 10	3.49E - 11	...	2.39E - 11	1.08E - 10	8.51E - 12	3.28E - 11	4.42E - 12
3.....	2.26E - 11	2.11E - 10	3.27E - 11	...	2.42E - 11	1.11E - 10	9.27E - 12	3.54E - 11
4.....	1.14E - 10	1.76E - 11	1.83E - 10	3.01E - 11	...	2.50E - 11	1.13E - 10	9.40E - 12
5.....	1.14E - 11	9.03E - 11	1.69E - 11	1.62E - 10	2.93E - 11	...	2.45E - 11	1.15E - 10
6.....	5.94E - 11	1.23E - 11	7.34E - 11	1.52E - 11	1.49E - 10	2.75E - 11	...	2.37E - 11
7.....	1.31E - 11	4.23E - 11	1.08E - 11	6.31E - 11	1.35E - 11	1.40E - 10	2.58E - 11	...
8.....	2.23E - 11	1.04E - 11	3.29E - 11	9.17E - 12	5.70E - 11	1.23E - 11	1.34E - 10	2.42E - 11
9.....	7.36E - 12	1.47E - 11	8.33E - 12	2.77E - 11	8.17E - 12	5.32E - 11	1.15E - 11	1.29E - 10
10.....	6.53E - 12	5.36E - 12	1.11E - 11	7.06E - 12	2.47E - 11	7.43E - 12	5.06E - 11	1.08E - 11
11.....	3.20E - 12	4.12E - 12	4.25E - 12	9.22E - 12	6.17E - 12	2.27E - 11	6.88E - 12	4.86E - 11
12.....	1.61E - 12	2.34E - 12	3.08E - 12	3.54E - 12	8.10E - 12	5.53E - 12	2.13E - 11	6.47E - 12
13.....	1.43E - 12	1.04E - 12	1.82E - 12	2.55E - 12	3.06E - 12	7.31E - 12	5.05E - 12	2.01E - 11
14.....	4.75E - 13	1.02E - 12	8.08E - 13	1.48E - 12	2.20E - 12	2.71E - 12	6.17E - 12	4.68E - 12
15.....	6.22E - 13	3.59E - 13	7.65E - 13	6.54E - 13	1.25E - 12	1.95E - 12	2.45E - 12	6.23E - 12
16.....	2.45E - 13	4.28E - 13	2.72E - 13	6.04E - 13	5.47E - 13	1.09E - 12	1.76E - 12	2.25E - 12
17.....	2.52E - 13	1.72E - 13	3.13E - 13	2.14E - 13	4.92E - 13	4.71E - 13	9.63E - 13	1.61E - 12
18.....	1.04E - 13	1.72E - 13	1.25E - 13	2.37E - 13	1.73E - 13	4.12E - 13	4.11E - 13	8.67E - 13
19.....	1.04E - 13	6.88E - 14	1.22E - 13	9.56E - 14	1.86E - 13	1.43E - 13	3.53E - 13	3.62E - 13
20.....	3.75E - 14	6.85E - 14	5.04E - 14	8.94E - 14	7.81E - 14	1.51E - 13	1.23E - 13	3.10E - 13

minimum necessary to describe CS-H₂ (Chapman & Green 1978). Attempts to fit this surface by expanding the angle dependence as usual in a Legendre polynomial series were unsatisfactory, and a more involved procedure, which included polynomial interpolation of the angle dependence, was employed (Bieniek & Green 1981). These procedures were thought to be adequate for studying high-temperature collisions and, in particular, for calculating the relative size of vibrational compared with pure rotational excitation rates, which is important for understanding the maser pump mechanism; they may not be adequate for calculating the relative size of different rotational excitation rates at low temperatures.

The present study calculated low-temperature rotational excitation rates using methods similar to those used for CS-H₂. The interaction potential was obtained from the electron gas model interaction of Bieniek & Green (1981) with the SiO internuclear distance fixed near its equilibrium value. This rigid rotor portion of the potential was available for nine orientations, $\theta = 0^\circ, 15^\circ, 30^\circ, 60^\circ, 90^\circ, 120^\circ, 150^\circ, 165^\circ$, and 180° , which was inadequate to determine a converged Legendre expansion as required by the scattering calculations. Therefore, values for four additional angles were generated by interpolation to give θ -values spaced approximately every 15° . In particular, it was assumed that $\log [V(\theta) + \epsilon]$ is a linear function of $\cos \theta$ between computed points to obtain values at the midpoints of available $\cos \theta$ values. For distances where the potential is negative (attractive) for some angles, all points were shifted up by ϵ to make the argument of the logarithm positive by at least 10 cm^{-1} . For each of the resulting 13 angles, the potential was extrapolated to shorter distances by fitting an exponential, $V(R, \theta) = A(\theta) \exp [-\beta(\theta)R]$, to the points at $R = 3.5$ and 3.75 bohr. Finally, a 12 term Legendre polynomial expansion was obtained by a least-squares fit to the 13 orientations (Green 1977b). As for CS-H₂, cross sections among rotational levels to $J = 20$ were obtained within the coupled states approximation, again assuming that the H₂ is constrained to its lowest, $J = 0$, rotational level. Calculations were done for a number of energies up to about 1800 K and included as many of 36 rotational levels to ensure convergence of cross sections. These were averaged over Boltzmann distributions to obtain rate constants for temperatures between 20 and 300 K.

Representative values are given in Tables 5 and 6 for CS and SiO, respectively, at a kinetic temperature of 250 K.⁵

⁵ The complete data sets, which include temperatures from 20 to 300 K and all rotational levels through $j = 20$, may be obtained from S. Green. Requests may be sent electronically via the BITNET network to AGXSG@NASAGISS or via INTERNET to AGXS@NASAGISS.GISS.NASA.GOV.

REFERENCES

- Bachiller, R., Cernicharo, J., Martin-Pintado, J., & Tafalla, M. 1990, *A&A*, 231, 174
 Bachiller, R., Martin-Pintado, J., & Fuente, A. 1991, *A&A*, 243, L21
 Bieniek, R. J., & Green, S. 1981, *Chem. Phys. Lett.*, 84, 380
 ———. 1983, *ApJ*, 265, L29
 Braun, R., & Strom, R. G. 1986, *A&AS*, 63, 345
 Burton, M. G., Brand, P. W. J. L., Geballe, T. R., & Webster, A. S. 1989, *MNRAS*, 236, 409
 Burton, M. G., Hollenbach, D. J., Haas, M. R., & Erickson, E. F. 1990, *ApJ*, 355, 197
 DeNoyer, L. K., & Frerking, M. A. 1981, *ApJ*, 246, L37
 Draine, B. T., Roberge, W. G., & Dalgarno, A. 1983, *ApJ*, 264, 485
 Fesen, R. A., & Kirshner, R. P. 1980, *ApJ*, 242, 1023
 Goldsmith, P. F. 1972, *ApJ*, 176, 597
 Green, S. 1975, *ApJ*, 201, 366
 ———. 1977a, *Chem. Phys. Lett.*, 47, 119
 ———. 1977b, *J. Chem. Phys.*, 67, 715
 Green, S., & Chapman, S. 1978, *ApJS*, 37, 169
 Hartquist, T. W., Oppenheimer, M., & Dalgarno, A. 1980, *ApJ*, 236, 182
 Herbst, E., & Leung, C. M. 1989, *ApJS*, 69, 271 (HL)
 Herbst, E., Millar, T. J., Wlodek, S., & Bohme, D. K. 1989, *A&A*, 222, 205
 Hollenbach, D. J., & McKee, C. F. 1980, *ApJ*, 241, L47
 Huang, Y.-L., Dickman, R. L., & Snell, R. L. 1986, *ApJ*, 302, L63
 Iglesias, E., & Silk, J. 1978, *ApJ*, 226, 851
 Irvine, W. M., Goldsmith, P. F., & Hjalmarson, A. 1987, in *Interstellar Processes*, ed. D. S. Hollenbach & H. A. Thronson (Astrophys. and Space Sci. Library), 561
 Kwan, J. 1977, *ApJ*, 216, 713

- Langer, W. D., & Graedel, T. E. 1989, ApJS, 69, 241
London, R., McCray, R., & Chu, S. 1977, ApJ, 217, 442
Martin-Pintado, J., Bachiller, R., & Fuente, A. 1992, A&A, 254, 315
Mitchell, G. F. 1984a, ApJ, 287, 665
———. 1984b, ApJS, 54, 81
Mitchell, G. F., & Deveau, T. J. 1983, ApJ, 266, 646
Monteiro, T. S. 1985, MNRAS, 214, 419
Neufeld, D. A., & Dalgarno, A. 1989, ApJ, 340, 869
Parkes, G. E., Charles, P. A., Culhane, J. L., & Ives, J. C. 1977, MNRAS, 179, 55
Silk, J., & Solinger, A. 1973, Nature Phys. Sci., 244, 101
Thomas, L. D., Kraemer, W., & Diercksen, G. H. F. 1980, Chem. Phys., 51, 131
Turner, B. E. 1973, Ap&SS, 29, 247
———. 1991a, ApJ, 376, 573
———. 1991b, ApJS, 76, 617
Turner, B. E., Friberg, P., Irvine, W. M., Saito, S., & Yamamoto, S. 1990, ApJ, 355, 546
Turner, B. E., & Lubowich, D. A. 1991, ApJ, 381, 173
van Dishoeck, E. F., & Black, J. H. 1988, ApJ, 334, 771
White, G. J., Rainey, R., Hayashi, S., & Kaifu, N. 1987, A&A, 173, 337
Ziurys, L. M., Friberg, P., & Irvine, W. M. 1989b, ApJ, 343, 201
Ziurys, L. M., Snell, R. L., & Dickman, R. L. 1989a, ApJ, 341, 857